

THESIS FOR THE DEGREE OF LICENTIATE OF ENGINEERING

Prerequisites for Efficient Programming of RFID Inlays in Reactive Near Field

Markus Frank



Department of Microtechnology and Nanoscience
CHALMERS UNIVERSITY OF TECHNOLOGY
Göteborg, Sweden 2016

Prerequisites for Efficient Programming of RFID Inlays in Reactive Near Field
MARKUS FRANK

© MARKUS FRANK, 2016.

Licentiatavhandlingar vid Chalmers tekniska högskola
Technical report No. MC2-334
ISSN 1652-0769

Micro and Nano Systems Group
Electronics Material and Systems Laboratory
Department of Microtechnology and Nanoscience
Chalmers University of Technology
SE-412 96 Göteborg, Sweden
Telephone + 46 (0) 31 - 772 1000

Cover: The optimization problem of reactive near field coupling between coupler geometry (CG) and inlay geometry (IG).

Typeset by the author using L^AT_EX.

Printed by Chalmers Reproservice
Göteborg, Sweden 2016

To my loved ones, Gustav, Vilhelm and Linda

Abstract

The electromagnetically isolated programming of unique user IDs, into the transponder memory of UHF RFID inlays, is essential for successful operation in the RFID inventory process. Bar code printers enabled for RFID represent a typical environment of such programming. They are usually equipped with an RFID interrogator and a reactive near field (RNF) coupler. Bar code printers, in particular those for industrial use, consist of compact robust metallic media housings. This environment fundamentally changes the electromagnetic properties of RFID inlays, nominally designed for operation in the far field. One fundamental requirement put on the coupler design is the strong mutual electromagnetic interaction towards RFID inlays with arbitrary antenna geometries, yet still completely isolated from neighboring inlays, being as close as a couple of millimeters apart. Another requirement is efficient coupling despite strong non-linearity of the transponder chip for increased drive power levels.

This thesis treats the prerequisites for an adaptive solution of geometry independent RFID inlay programming in reactive near field.

The work is divided into two distinct parts. The first part addresses the non-linear behavior of RFID transponder chips under source impedance and drive level shift. A measurement method with modulated stimuli is developed from which a figure of merit (FOM) is extracted, including the $|\Delta\Gamma|$ -value, a common performance parameter found in the RFID community. A dual probe connection method is introduced, enabling the characterization of RFID transponder chips from several vendors having different size parameters. An approximate ideal clipping model is developed, enabling power swept measurements with a linear vector network analyzer (VNA).

In the second part the differential transmission line loop (DTLL) is presented as novel coupling element for high efficient programming of RFID inlays in reactive near field (RNF). Results for simple super elliptic loop geometries show strong magnetic coupling towards a number of different inlay geometries, utilizing the current inductive loop of the inlay. The inductive loop is common for virtually all inlay types, making the DTLL a strong candidate as coupling element in future adaptive coupling technologies. In particular the DTLL offers design flexibility both in component choice and geometry, suitable for further element optimization.

Keywords: DTLL, FOM, Phase compensation, RFID, RNF, Source Impedance Shift, UHF.

Acknowledgments

This project would not have been possible without the support and decision of initiation from my company Sato. Many thanks are directed towards Mats Hedberg, my supervisor and cite manager of Sato Techno Lab Europe, for motivating the industrial problem as a scientific one towards the management in Japan.

Many thanks are directed towards Professor Peter Enoksson, head of the EMSL Micro and Nanosystems group at MC2 and my main supervisor, for accepting me, a total stranger from industry and long time out of academia, as a PhD student in his group. Peter has an open attitude towards new problem statements, and if it wouldn't have been for people like him, the project would probably never have been initiated from the university side. I'm also thankful for the many useful comments I received from Peter in writing this thesis.

My co-supervisor Mattias Thorsell at MEL came in late in the project, which suffered from organizational challenges with time delays as consequence, but we managed to find a good recipe for qualitative publications. His straight forward manner towards me, good academic overlook of the project in its entirety, with a road map towards the final goal, has helped pushing the project forward in a constructive way. I am extremely impressed of his qualifications as a reviewer of my texts, and very thankful for his involvement in the project.

Many warm thanks go out to Robert Eskilsson and his colleagues at Rohde & Schwarz Sweden and Germany for loan and support of instrumentation.

Although I am not present most of the time in my group at EMSL, at those times I am, I experience warm friendship and good company from Henrik, Sofia, Elof, Per, Amin and Volodymyr.

My beautiful wife has patiently and quietly watched me spending excessive time, battling with difficult theoretical problems, completely missing out on the well needed support of the family. Without her warm caring of our lovely sons, Gustav and Vilhelm, while I was absent, both mentally and physically, this project would also not be possible. Unfortunately we have not yet arrived at the goal.

Except Sato Techo Lab Europe, being my employer, this thesis work also gains financial support from the Swedish Research Council.

Markus Frank
Göteborg, Stråvalla 2016

List of Publications

Appended papers

This thesis is based on the following appended papers:

Paper A. M. Frank, M. Ferndahl, M. Thorsell and P. Enoksson, “Differential Impedance Measurement Method of RFID Transponder Chips at UHF,” in *2013 43rd European Microwave Conference (EuMC)*, 6-10 October, Nuremberg, Germany, 2013, pp. 68-71.

Paper B. M. Frank, M. Thorsell, and P. Enoksson, “Shifted Source Impedance and Non-Linearity Impact on RFID Transponder Communication for Drive Level Offsets,” *IEEE Transactions on Microwave Theory and Techniques*, vol. 64, no. 1, pp. 299–309, January 2016.

Paper C. M. Frank and P. Enoksson, “Phase Compensated Transmission Line for Leakage Field Coupling in UHF RFID Applications,” in *2013 7th European Conference on Antennas and Propagation (EuCAP)*, 8-12 April, Gothenburg, Sweden, 2013, pp. 1702-1706.

Paper D. M. Frank, M. Thorsell, and P. Enoksson, “Differential Transmission Line Loop for RFID Reactive Near Field Coupling,” *Manuscript*.

List of Acronyms

CG	–	Coupling Geometry
DTLL	–	Differential Transmission Line Loop
DUT	–	Device Under Test
EU	–	Extension Unit
FEM	–	Finite Element Method
FOM	–	Figure Of Merit
GPIB	–	General Purpose Interface Bus
GUI	–	Graphical User Interface
IG	–	Inlay Geometry
MATLAB	–	MATRIX LABORATORY
RF	–	Radio Frequency
RFID	–	Radio Frequency IDENTIFICATION
RFCW	–	Radio Frequency COMMUNICATION WINDOW
RFW	–	Radio Frequency WINDOW
SCPI	–	Standard Commands for Programmable Instruments
SG	–	Signal Ground
TDM	–	True Differential Mode
TRL	–	TRANSMISSION LINE
VNA	–	Vector Network Analyzer

Contents

Abstract	v
Acknowledgments	vii
List of Publications	ix
List of Acronyms	xi
1 Introduction	1
1.1 Principle of an RFID system	1
1.2 Programming of unique user identities	2
1.3 Inside the printer: The RF window	3
1.4 Current RNF coupler technology	6
1.5 The step towards research	7
1.6 Organization of thesis	8
2 Characterization of RFID Transponders	9
2.1 Probe connection methods	9
2.2 Vertical alignment for dual probe method	10
2.3 Steps in measurement procedure	11
2.4 Comparison of probe connection methods	11
2.4.1 Individual repeatability	11
2.4.2 Deviation linear region	12
3 Non-linear characterization	15
3.1 Design and characterization of transponders: A review of reported work	15
3.2 General non-linear behavior	16
3.3 The approximation	20
3.4 Behavioral model	21
3.5 Figure of merit calculation	24
3.5.1 Mismatch theory for source impedance shift	25
3.5.2 The $ \Delta\Gamma $ -value	27
3.5.3 Figure of merit	28
3.6 Measurement system	30
3.6.1 Setup	30
3.6.2 Device under test	32
3.6.3 Matched condition	33

3.7	Verification of repeatability	33
3.8	Verification of source independency	34
3.9	Post analysis	36
3.10	Measured FOM	37
3.11	Conclusions FOM characterization	41
4	The linear channel between transponder and interrogator	43
4.1	Two aspects on programming RFID inlays	43
4.2	Q -value reduction	44
4.3	Sensitivity enhancement	45
5	Spatial selection by phase manipulation	49
5.1	Lumped component phase compensation	49
5.2	Predicted frequency dependency	51
5.3	Simulated results and fabrication	53
5.4	RFID profiling results	54
6	The differential transmission line loop as efficient coupling element	57
6.1	The inlay inductive loop as coupling target	57
6.2	Properties of the DTLL	58
6.3	Design	58
6.4	Results	61
7	Conclusions and future work	65
A	A short review of the RFID protocol	67
A.1	Baseband	67
A.2	Wake-up signal	68
A.3	Estimation of maximum required recording time	69
A.4	Minimum required system bandwidth	70
B	Circle theory	71
C	Graphical user interfaces	73

Chapter 1

Introduction

1.1 Principle of an RFID system

RFID (Radio Frequency IDentification) at ultra high frequencies (UHF) is becoming a standard complement to common bar codes for the tracking of objects in supply chain management [1]. The general RFID system, as illustrated in Figure 1.1, consists of multiple interrogators and multiple antennas linked together in a network, with the purpose of inventory and data collection in a population of data carriers.

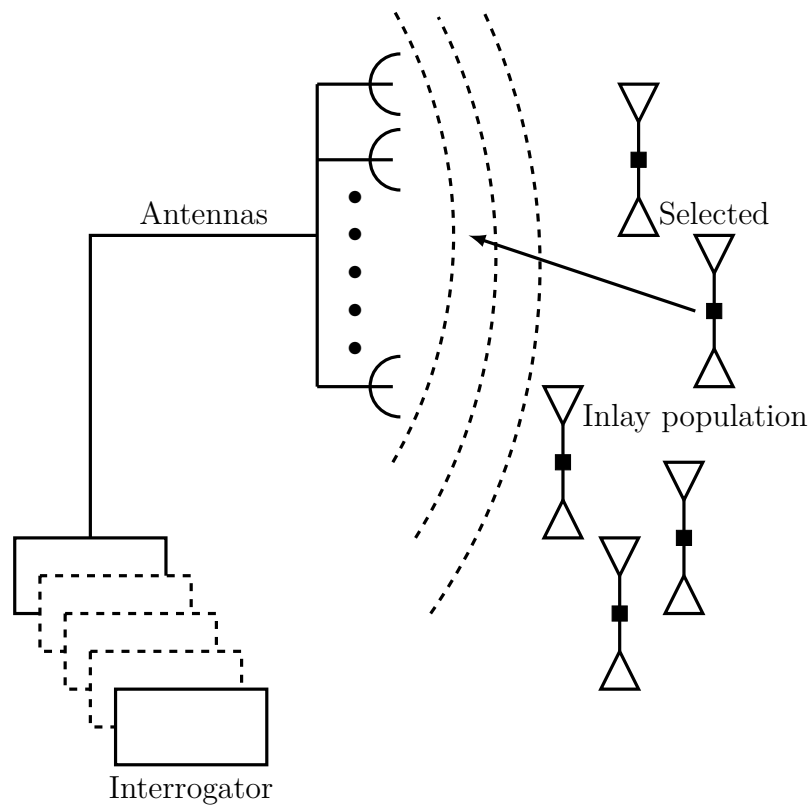


Figure 1.1: Principle of a general RFID system.

The data carriers are realized as passive or active (battery assisted) tags. A tag is an antenna connected to a transponder, which receives, stores and replies information. A special case of an RFID tag is an RFID inlay, where the antenna is a flexible metallic film. The term inlay, as opposed to tag, which is more general, will be used throughout this thesis and only passive transponders are considered.

The principle of communication is based on the broadcast of a radio signal, subject to a digital modulation format containing commands, from the interrogator. The broadcast is followed by the inlay replies, of which only one selected at a time may respond, also called half duplex communication. The inlay antenna presents the frontend towards the energizing RF field and is one of the conditions for the amount of energy needed by the transponder to operate properly. RF energy absorbed by the antenna will feed the transponder chip, which converts this energy to a DC bias for digital circuitry.

The backward communication link from the inlay to the radio is based on backscattering, in which the inlay reflects and modulates a part of the radio signal back to the interrogator. The protocol enables a population of multiple RFID inlays, each with a unique ID, to be located in the same radio field. The singulation of inlays is done through an inventory process, performed by the interrogator [2].

At UHF and higher frequencies the free space wavelength is of a size order where it is possible to design antenna structures which fit into standard bar code media. Since the antenna is tuned for a propagating wave, read and write distances of several meters can be achieved.

There are also RFID tags operating at lower frequencies such as HF (High Frequency). In this case energy is transferred by pure inductive coupling. The “antenna” in this case is more or less an inductive coil of a number of turns which is connected to the transponder. This technology is characterized by shorter read and write distances but more robust RF near field performance.

1.2 Programming of unique user identities

A necessary task in an RFID system is the programming of unique user identities to the inlay transponders. This is a critical and essential procedure, since without unique user IDs inlays are useless in the RFID inventory process. Note that the programming of user IDs precedes the actual end user application, which today is mostly concerned with inventory of unique data carriers. One common environment where the programming is carried out, is an RFID enabled printer, which is a typical representative for the electrical conditions being of primary interest in this thesis. The task of an RFID enabled printer is not only to print visual bar code label media. The RFID label printing command also contains RFID commands containing information intended for storage in the inlay transponder memory. In order to achieve this the printer is equipped with coupler technology of programming unique user identification into the transponder memory of RFID inlays.

In the end user application, for which the inlay antenna is designed, the inlay, interrogator antenna and other objects are located some distance apart. Spatial

regions with these distances between objects are known as the far field or radiating near field. Certain electrical properties of the inlay, interrogator antenna and other objects will then not be electromagnetically affected by the presence of each other. If the distance is close, such as a fraction of the radiating wavelength, their electrical properties are not independent of each others physical structure any longer. In other words, they are located in the reactive near field (RNF) of each other. One such case is found in RFID enabled bar code printers. A critical condition for satisfactory operation of the transponder, especially at high frequencies, is the connection of the antenna to the chip. The mismatch between the antenna port and the transponder RF frontend electrically quantifies the relative amount of power transferred between the antenna and the transponder, given the connection between them. Looking into the antenna port when it electromagnetically interacts with external objects located close, can electrically be seen as some unknown source, which depends on the environment the inlay is located in. This means that the default scenario in a propagating environment, usually for which the antenna was initially designed, does not exist anymore.

The only way to transfer information from the interrogator to the inlay transponder is over the air protocol by the near field coupler arrangement [3–6]. Since this needs to be done in an electromagnetically isolated manner to individual inlays, where the repeated distance between tag neighbors may be very small, it puts special requirements on the coupler, as shown schematically in Figure 1.2.

The geometry of inlays may be very different so in a sense transparency towards inlay geometry is required. Furthermore, the transponder presents a strong non-linearity for an increased RF power drive level from the interrogator. The non-linearity has impact on the electrical mismatch, in the interface between the transponder RF frontend and the inlay antenna. Therefore the drive level must be kept sufficiently low, as to allow stable communication between interrogator and inlay, yet still being high enough as to exceed the modulation threshold level. From another aspect, drive levels are also required to be as low as possible, in order to assure electromagnetic isolation between neighboring inlays. In summary these constraints put efficiency requirements on the RNF coupling between coupler and inlay antenna. Clearly, the combination of a dense inlay environment and big variety of geometry presents challenges in coupler design.

1.3 Inside the printer: The RF window

The transparent programming of RFID inlays in a printer environment motivates the research presented in this thesis. Consider the usual test scenario in an RFID printer. The media path in the printer cavity may be regarded as some curved path. Seen from the RF perspective the vertical distance between the inlay and some structure which is not part of the media but which also conforms to the path, is very small. It can be assumed that this distance is also electrically small, in terms of the wavelength of the carrier wave energizing the inlay. Hence, there is no loss in generality when the media path is straightened out. The problem of profiling inlays

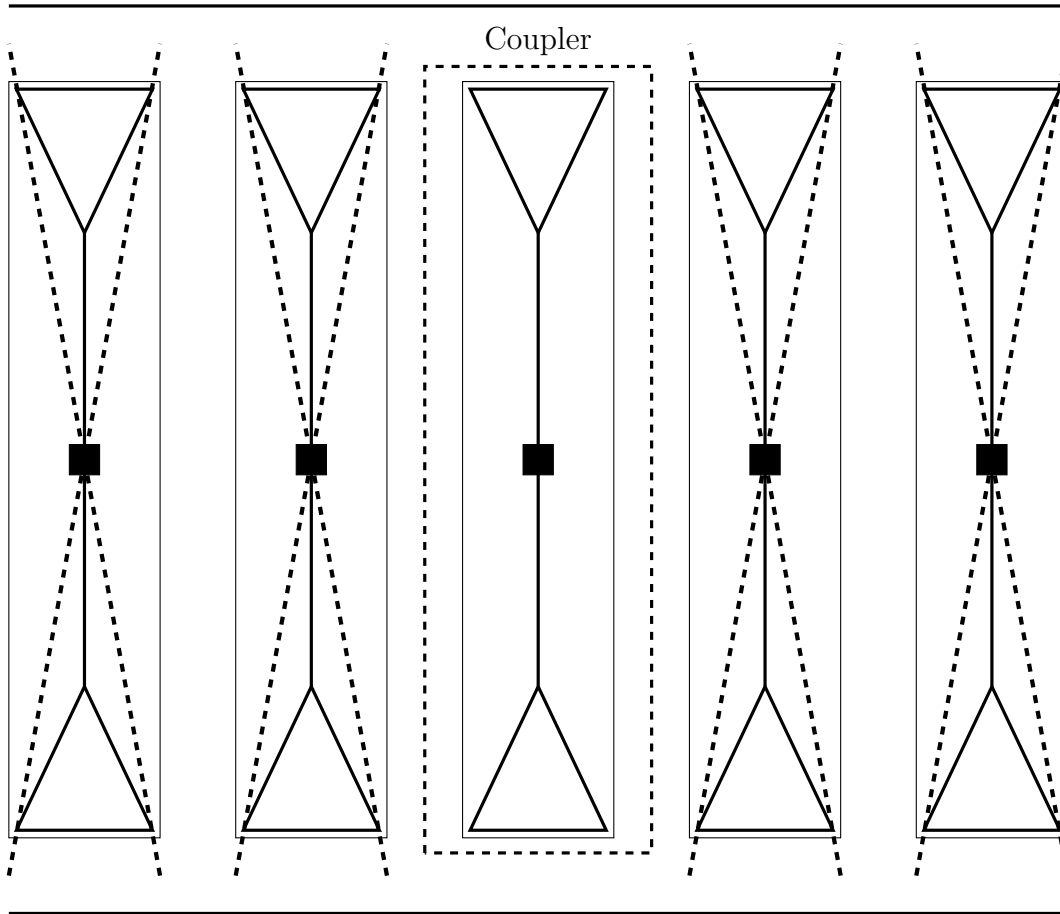


Figure 1.2: Illustration of the isolated programming problem in a printer cavity.

in terms of the strength of RF coupling to a coupling structure is then reduced to two dimensions in the plane. The plane is denoted xy -plane, i.e. along the width and length dimensions of the stretched media path, see Figure 1.3.

When an RFID inlay travels along the media path in a printer cavity equipped with an RNF coupler at a fixed position, there will usually be one or several regions where the inlay may be programmed. These are regions with an RF coupling level between inlay and coupler reaching a certain threshold and above, where the transponder has a high enough bias to operate. Regions where the coupling is so low that no communication over the RFID protocol can be detected for any RF power level, in a fixed interval out from the interrogator, are known as NOTAG regions. The entire response from NOTAG to NOTAG region is known as the RF Window (RFW). This may consist of discontinuous sub regions with any type of response, provided there is a detection on the interrogator side. As the inlay enters the RFW, the mismatch becomes a function of power level, due to the non-linear nature of the transponder. Within the RFW certain regions can be detected where both read and write communication is stable, denoted RF Communication Windows (RFCW).

If the coupler is a rigid structure, such as for example a set of transmission lines used for leakage field coupling, the shape of the RFW will be determined by the

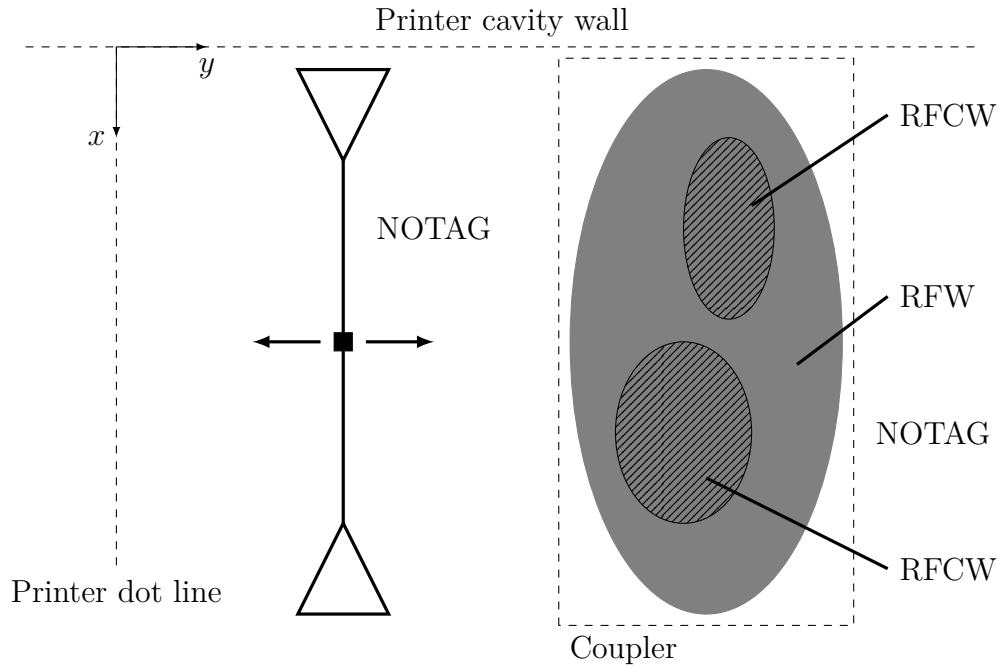


Figure 1.3: Illustration of inlay movement in the printer coordinate system.

mutual interaction between the inlay and the coupler [3–5, Paper C]. This is an important observation. In a sense the combination of inlay, coupler and other objects of the printer exhibits a certain “profile” of programmability, which is unique for the particular inlay geometry being tested. As soon as the inlay geometry changes, the profile also changes. The term “inlay profiling” is commonly used in the RFID printer community.

Another important observation is the dependency of profile on RF output power from the interrogator. The initial linear characteristics of the transponder for lower power levels will imply an envelope of the RFW which spatially always looks the same. However if the power level is increased, so that the transponder enters the non-linear region, certain phenomena can be identified, where read and write performance may even break up. Also the relationship between read and write power thresholds generally changes for excessive power levels. In the linear case there is always a certain offset between read and write power threshold, which generally changes for higher power levels. Figure 1.3 should be understood as the situation for a fixed power level. An example of an RFW profile, resulting from the RFID test environment, is shown in Figure 1.4.

In this case the x -coordinate is fixed, but the RF power is swept within an interval. The abscissa, labeled y , indicates the position along the media path. The ordinate, labeled P_{AVS} , indicates the available output power from the interrogator. The different types of dots indicate quality of communication, such as read only with empty blue circles, and full read/write performance with black filled circles.

The testing illustrated in Figure 1.4 includes the whole component chain, such as interrogator transceiver, wireless channel with electromagnetic interaction between

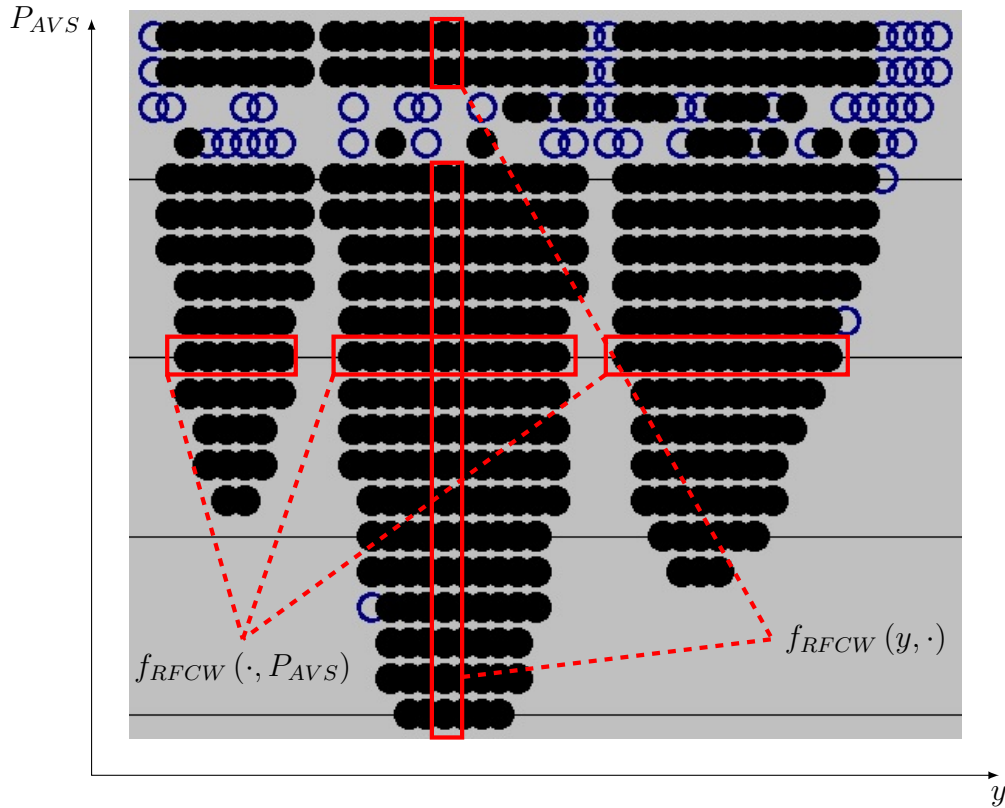


Figure 1.4: Example of RF window profile from test performed inside a printer cavity. Note the discontinuity of the RFCWs.

inlay antenna and printer cavity, and chip-nonlinearity. From the observation of the profile it is generally difficult to exactly determine the different components respective contributions to the profile shape. Furthermore, the testing is performed over the RFID protocol, where software parameters may also have an impact. It is concluded that, for sure, a well matched RNF coupler system will result in desirable properties, such as better continuity in the RFCW profile and wider RFCW regions at lower RF power levels, closer to the threshold.

1.4 Current RNF coupler technology

Conventionally, two types of RNF technologies are used to encode RFID tags (inlays) in RNF, which are, in principle, suitable for being fitted into printer cavities. The first type are static coupler designs which employ a rigid coupler circuit, such as a transmission line circuit on a PCB (printed circuit board). Since the circuit is rigid and inlay geometries generally have very high variability in form factor, the RF coupling behavior between coupler and inlay will also have a high variability. Hence, for each inlay type RFW profiles can be uniquely identified, such as the one shown in Figure 1.4 [6].

Apart from rigid coupler circuits, an alternative second type of RNF coupler technology are adaptive coupler designs with external control, also called semi-adaptive couplers [7, 8]. In this technology, the coupler structure is split up into several coupling elements, such as an array. Each element is individually controlled by some external circuit and software. This means that for each type of inlay, regardless of its geometry, an adaptation can be performed in that only elements for that particular inlay form factor are activated, in order to achieve an optimum coupling. In the ideal case, optimum coupling regardless of inlay form factor can be achieved by having prior knowledge of which elements to activate. In order to get this information about which cells need to be activated, knowledge of the inlay profile is required. Therefore, a scanning process of unknown inlay geometries is necessary. The information obtained by scanning can be stored in a memory so that each inlay type only needs to be scanned once. Nevertheless, for each new inlay type the process has to be repeated. Therefore, an adaptive coupler of said type is not operable as a stand alone component. It must be accompanied by a software solution containing the necessary algorithms for the scanning process, required for external control of the elements to be activated, possibly involving the whole printer system.

Regardless of which coupler type is considered, the element, whether it is in single configuration making up the whole coupler or in an array configuration, is generally a non-optimized design, when the larger family of inlay geometries is taken into account. In the semi-adaptive case the solution is the controlled excitation of the individual elements for optimized RNF coupling field, where the imperfection of the individual element is overcome.

The common drawback for both types of the above described conventional coupler types is the need for calibration, in order to adapt the coupling arrangement to a particular inlay to be encoded, before an actual encoding can be performed. Either, for the static coupler type, positioning of the inlay for optimum coupling must be known, or, for the semi-adaptive coupler type, the inlay profile formation must be obtained and stored. Hence, there is a need for a scanning functionality in order to know the inlay profile. Furthermore, if the resolution of the coupling element array is not high enough, inlay types may still exist which cannot be encoded and the required resolution for any future inlay type may be hard to determine.

1.5 The step towards research

A first step towards an optimal RNF design, would be to first electrically characterize fixed components such as interrogator and transponder RF front ends. This will be the starting point of the presented research, of which interrogator related investigations are not part. Rather focus is put on transponders from different vendors. The next step is the design of an efficient RNF coupler technology. The term efficient should be interpreted as a strong electromagnetic interaction between inlay and coupler, yet still, being spatially selective. Embedded in this design problem is the electrical property of transponder response to shifted source impedance, which links back to the first step.

The research methods presented in this thesis are based on the distinct identifiable interface between the transponder RF frontend and the inlay antenna port. The interface naturally divides up the problem into:

- A non-linear circuit related part
- A linear field theory related part

The circuit related part is concerned with the wired measurement, characterization and modeling of transponders existing on the market, i.e., this part is not design related. Rather it deals with the study of existing designs. The transponder chips characterized are so small, in terms of the guided wavelength of a system supplying them with electrical power, that wavelength phenomena can be neglected. Rather these components can be treated as pure electrical circuits with non-linear characteristics.

The field theoretic part is concerned with the design of efficient coupling structures, intended for RNF. This is a pure linear problem, but with strong dependency on wavelength. Phase manipulation will be a term reappearing at several occasions in this thesis.

At this point a general remark is at hand, striving for the transparency towards inlays. Inlays consist of geometries and transponder chips from varying vendors. Consequently, rather common electrical properties for transponder chips and inlay antennas are considered, without delving too much into any specific topology.

1.6 Organization of thesis

This thesis is organized as follows. Chapter 2 treats the electrical connection interface towards RFID transponders. Probed measurements are presented with results taken from Paper A. Chapter 3 starts with a general discussion around non-linearity in a first part. In the second part, which forms the core of this thesis, a figure of merit (FOM) for non-linear characterization of transponder chips is presented in detail. The chapter is concluded with a presentation of the measurement method and results. The material is taken from Paper B. Chapter 4 introduces the turn towards the more field theoretic topic of reactive near field couplers, with a discussion around Q -value reduction and sensitivity enhancement from two-port transformations. In chapter 5 the concept of phase compensated segmented transmission lines in the application of RFID reactive near field coupling is presented, with results taken from Paper C. In Chapter 6 the differential transmission line loop as efficient reactive near field coupling element for RFID profiling is presented, with results taken from Paper D. Conclusions and future work are covered in Chapter 7.

Chapter 2

Characterization of RFID Transponders

For the characterization of RFID inlays and more specifically RFID transponder chips, as mentioned in Section 1.5, the interface between the RF frontend and the antenna port is natural. It divides the transponder-antenna system into a non-linear circuit part and a linear field theoretic part.

From an electrical perspective of the discussion in the previous chapter, consider the characterization of transponders by means of wired measurements. The initial question is how a wired connection physically should be realized, which is flexible to a varying size factor of the transponder chip. Transponders from different vendors are generally different in size, but the electrical measurement method should be consistent, independent of vendor. Consistent here means that the measurement method should have no influence on certain electrical characteristics different chip types (different vendors) may have in common, for an accurate comparison.

2.1 Probe connection methods

In Paper A work is presented on bare wafer connection methods. Different transponder chip types have different distances between the connector pads. A single probe measurement method with fixed pitch distance between the probe tips would soon become useless, if the purpose is a comparison between a variety of chip types from different vendors. Typical pitch distances range between 25 and 1250 μm [9]. Still, a single probe connection was possible for one of the chip types, using the 50A-GS-400-DP miniature coaxial Picoprobe from GGB Industries with CS-14 calibration substrate [9]. This chip type serves as reference when comparing with a dual probe connection using the same probe type, as illustrated in Figure 2.1. The realization is shown in the bottom photo. In the left photo one of the probes is used for mechanical support only. In the right photo an example of a larger size factor chip type is shown, where the distance between pads (diagonally aligned) is bigger than the pitch distance of the probe.

Measurement data of complex impedance are taken from a Rohde & Schwarz® ZVA24 vector network analyzer (VNA) for the reference chip type. 10 individual

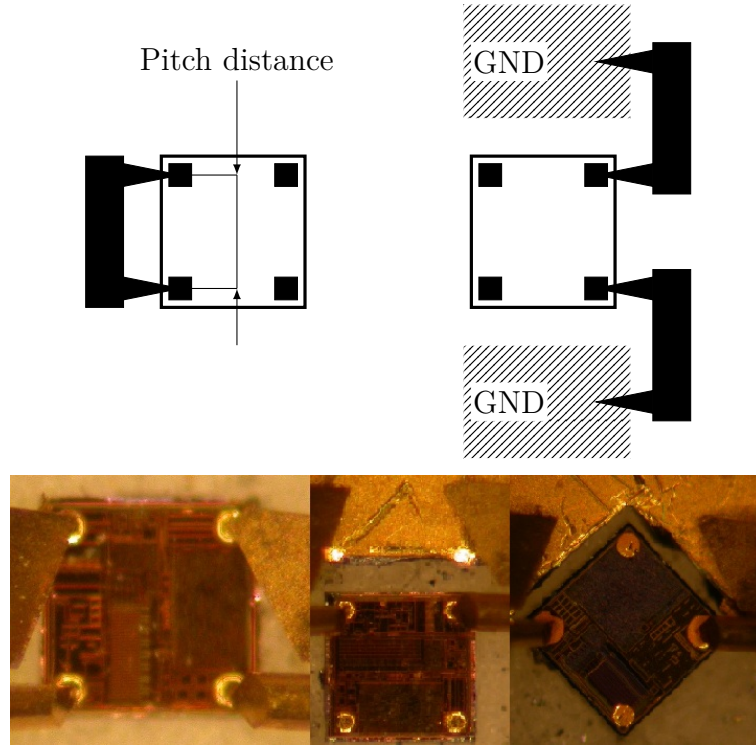


Figure 2.1: Top: Schematic illustration of single probe connection (left) as compared with dual probe connection (right) with common ground plane. Bottom: Realization.

chip samples are included to check repeatability. The calibration reference plane is at the probe tips using the calibration substrate. For power levels below approximately -10 dBm in a 50Ω system the transponder can be considered as being in a linear state. A linear state port power level is chosen for all measurements related to probe connection comparisons.

2.2 Vertical alignment for dual probe method

One of the challenges in the dual probe connection method was to establish a stable electrical connection of the signal tip and ground tip simultaneously. The situation is illustrated in Figure 2.2. The problem arises from the chip being a loose component, whereas the ground connection is established on a gold plated substrate not necessarily being of exactly the same height as the chip wafer. The wafer thickness of the transponder chips were measured and typical values range from 70 to 150 μm . Hence, big differences are seen. After several attempts the easiest way to establish a satisfactory connection proved to be the loose positioning on the bottom plate, to provide flexibility for manual adjustment of the chip with the probe tips themselves. The probe tips have some mechanical spring flexibility, which helps establishing the electrical contact. It is additionally recommended to use a probe

station with theta alignment, which was also a necessary requirement for the chip types having the biggest difference between wafer thickness and ground substrate.

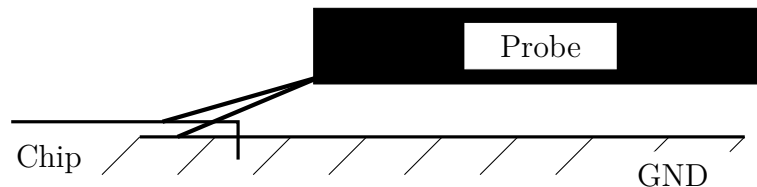


Figure 2.2: Illustration of vertical alignment (side view).

2.3 Steps in measurement procedure

The procedure consists of three steps. The first step is the single ended one-port connection with a single probe. The second step is the dual probe connection. In this case the true differential option in the VNA is used, which converts the two-port connection to a logical differential one-port. The source impedance in this case is 100Ω . Since the transponder is in a low power linear state, the calibration will hold also for this case. In the third step a tuner is inserted between the single ended one-port connection and the VNA.

The purpose of tuner insertion is to compare the de-embedded measured linear state impedance with the methods not using tuners, to verify the more general method, including an altered source impedance (source-pull). A de-embedding procedure based on three equations for three unknowns and reciprocity is used [10]. A pre-characterization method with calibration at the input of the tuners (coaxial plane) is chosen, instead of as in previous reported work, where calibration after the tuners was used [11]. This is done after the tuners have been set to the desired source impedance. Then the whole setting range of the tuners need not be measured.

2.4 Comparison of probe connection methods

2.4.1 Individual repeatability

For the reference chip type with size parameters compatible with all probe connection methods, initially power swept impedance data is taken for ten individuals. The one-port single ended, differential on-port and de-embedded connection are compared in Figure 2.3.

One individual deviates in all methods. This is due to an internal electrical difference for this particular individual. The exact nature of this deviation is unknown. Several measurements on the individual, however, showed a repeated behavior. Otherwise an overall good repeatability is seen. This stability is important, especially when several individuals and types are measured. The motivation of measuring several individuals is that a good real life representative is obtained after

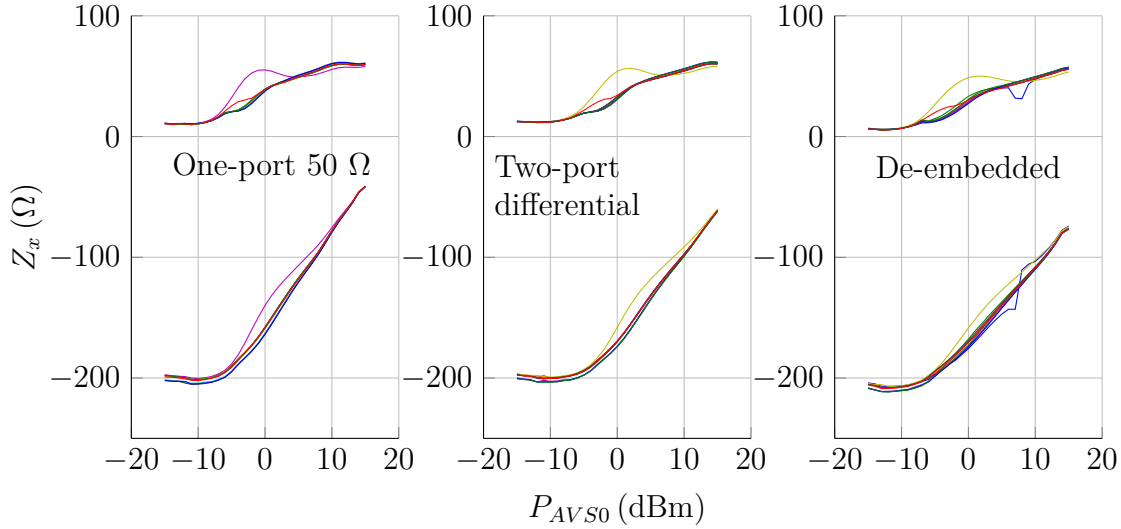


Figure 2.3: Measured impedance for 10 individuals of reference chip. Left: One-port (single probe/single ended). Middle: Two-port (dual probe) differential. Right: Two-port (dual probe) de-embedded.

averaging. It is also concluded that the inductance due to the distance between the probe tips connected to ground in the dual probe connection has negligible impact. FEM simulations verify this fact.

2.4.2 Deviation linear region

Figure 2.4 shows the zoomed linear region, taken as an average over the 10 individuals.

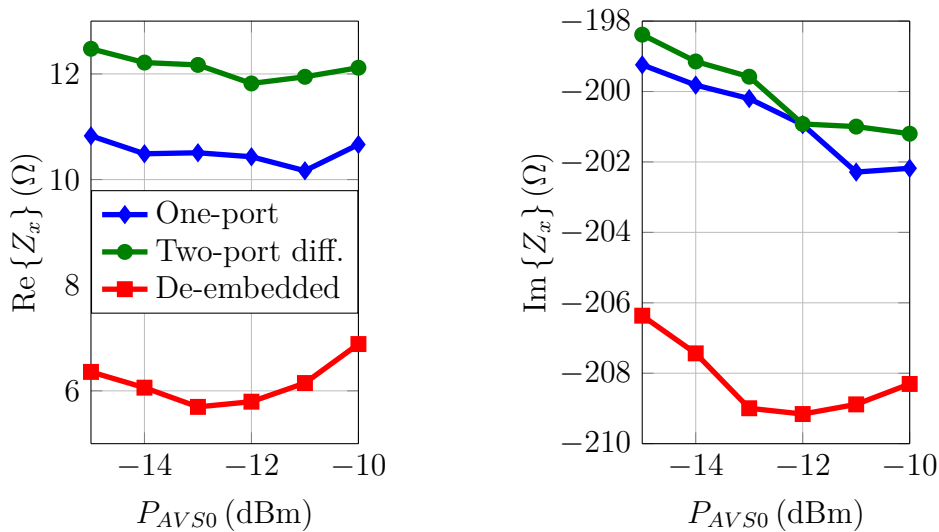


Figure 2.4: Impedance zoomed over linear region for average over individuals of reference chip.

It is observed that the de-embedding method deviates from the one-port and differential two-port. However, the number of loads in the pre-characterization is low. Yet still, from the results in Figure 2.4, the deviation using the method with three known loads is not considered to be significant. By introducing a larger number of known loads a more accurate characterization can be obtained, which may improve the agreement with the measurements performed directly at the probe plane. The equations are found in literature [10].

The one-port single ended and two-port differential measurement data agree well. This is also seen from carrying out several measurements on the same individual, where the obtained impedance value is stable. In the case of the reference type no significant differences could be seen between the single and dual probe connection.

The overall conclusion is that the dual probe connection has stable electrical characteristics, when lowering and lifting the probe tips a repeatable number of times, showing the usefulness for wired non-linear characterization, which will be the topic of the next chapter.

Chapter 3

Non-linear characterization

In the previous chapter a physical connection method suitable for on wafer measurements of RFID transponder chips was exploited. Importance of an electrically stable connection, combined with the flexibility of switching between individuals and different size factors, were addressed. With the questions of how to measure and how to connect answered, in this chapter follows a two part treatment of what to measure, being the main focus of gravity in this thesis. The first part will be a discussion around non-linearity in general and cautions to be taken, when carrying out measurements with linear vector network analyzers (VNA). In the second part a measurement method will be presented, providing the possibility of measuring complex impedance of RFID transponder chips within a pulse. A figure of merit (FOM) theory is presented and the chapter is concluded with measurement results. Initially a review of reported work in design and characterization of RFID transponders is presented.

3.1 Design and characterization of transponders: A review of reported work

Most research on RFID transponders reported today concerns the design and characterization of the RF frontend in discrete fixed source environments, rather than considering source impedance as a continuous free variable. The nominal operation of an RFID inlay takes place in such an environment. Hence, this is no great surprise.

A distinction of environments, where the source has less or more impact is well defined by the definition of RNF, propagating near field and far field [12, 13]. Of highest importance for an inlay is the performance of operation in the far field. The design and optimization of transponders is a big research topic [14–17]. Another extensive research topic treats the measurement and characterization of the transponder, by means of wired measurements. The fixed source impedance measurement of linear state transponders, using S -parameters, can be seen as a basic method [18, 19]. Still this is an important measurement, since mismatch performance is of the highest importance at the threshold level, where the transponder is in its linear state. A more advanced method consists of probed measurements of RFID

straps with a source-pull system, introducing the concept of shifted source impedance for matching purposes. In another method source impedance shift is introduced by the mutual interaction of antennas [20]. Research on non-linear characterization with measurement of harmonic contents is also reported [21]. An more enhanced non-linear characterization method is the capturing of wave form data [22]. No generalization is possible for a full characterization, but in this case certain fixed topologies need to be considered [23].

Another aspect on transponder characterization is the stimuli. Interrogator functionality, in particular the generation of a wake up signal, can be realized using a vector signal generator, as one exemplary method [11]. Another method is to integrate a commercial interrogator or an RFID tester in the measurement system [18].

The definition of a FOM is an important component in this thesis. One reported method, defining a FOM, takes into consideration not only the forward link in an interrogator/inlay system, but also the reverse link [24]. In other words an S -parameter network is defined, where however detuning effects from the inlay antenna on the interrogator antenna is approximated as negligible. Hence, the mismatch condition, due to RNF effects is not considered, other than that resulting from load compression.

The concept of arbitrary source impedance in RFID transponder performance evaluation is novel. From the literature study of reported work on the design and characterization of transponders a new field is identified, where an inlay is operated in an RNF environment which strongly deviates from the nominal case. This means that the design is a fixed parameter but knowledge is needed of the performance in the altered environment.

3.2 General non-linear behavior

The operation of an RFID tag in the reactive near field, such as in an RFID enabled printer cavity, is significantly different from far field or even propagating near field conditions [3–5]. The antenna port of an RFID inlay can be regarded as a complex source impedance presented towards the RFID transponder. In an altered RNF, such as a printer cavity, this impedance no longer consists of the antenna itself. Rather all objects with electromagnetic interaction surrounding the transponder are included. Hence, the assumption of fixed source impedance will generally not hold [13]. It rather changes continuously when the inlay moves along the media path and is difficult to predict. It may even be regarded as a free variable.

In addition to a shifting source impedance, non-linearity in the transponder is an inevitable component, which cannot be overlooked. Even for relatively low drive levels non-linearity has a strong impact. A measured example is shown in Figure 3.1.

The power sweep of the impedance and mismatch factor for two different transponder chips is plotted. The reference in this case is the same chip type as discussed in Chapter 2. The mismatch factor (also denoted M in this thesis), defined as

$$\tau = \frac{4R_s R_{xL}}{|Z_s + Z_x|^2} \quad (3.1)$$

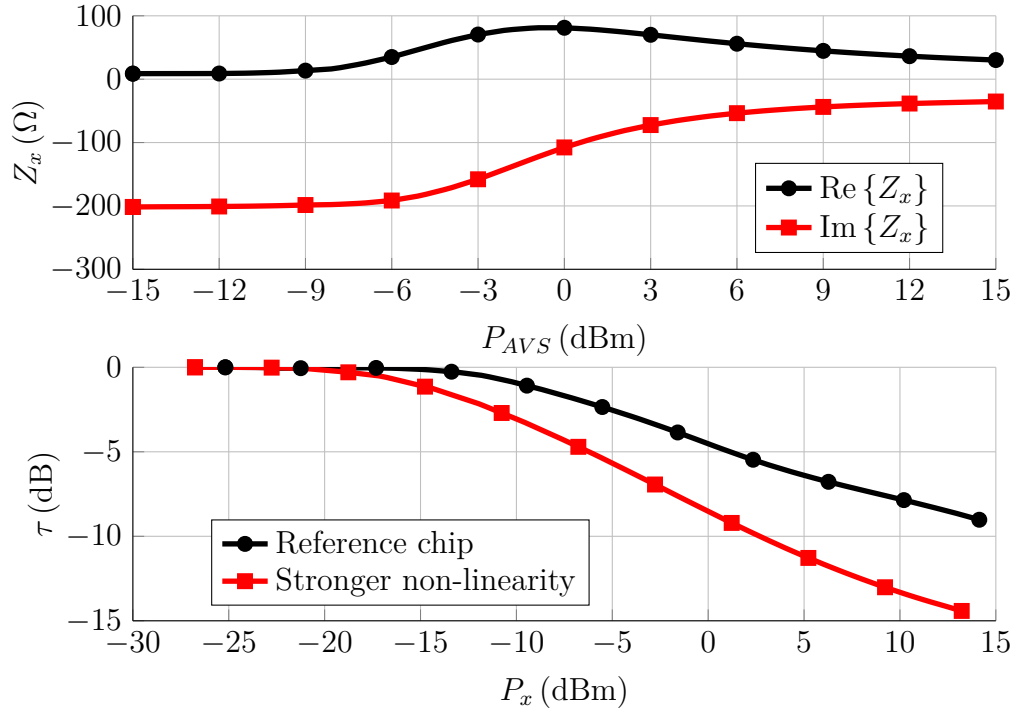


Figure 3.1: Examples of different degrees of non-linearity. Top: Power swept impedance in 100 Ω system. Bottom: Mismatch factor with source impedance set to conjugate match in linear state.

is plotted as function of delivered power. Since impedance data is initially available as function of available power, the available power is first mapped to delivered power as $P_x = \tau P_{AVS}$ and then (3.1) is used. Throughout this thesis P_x will denote the delivered power to the chip. From the definition of available power

$$P_{AVS} = \frac{|V_s|^2}{8\text{Re}\{Z_s\}} \quad (3.2)$$

a set of available power values in one impedance system can be mapped to an equivalent set of available power values in a different impedance system, given as

$$P_{AVS,2} \text{ (dBm)} = P_{AVS,1} \text{ (dBm)} + 10 \log_{10} \left(\frac{\text{Re}\{Z_{s,1}\}}{\text{Re}\{Z_{s,2}\}} \right). \quad (3.3)$$

If a shift in source impedance shift is presented by means of a two-port transformation, as shown in Figure 3.2, the S -parameters are added to the equation. In this case consider the source impedance $Z_{s,2}$ as seen at the output of the two-port. It is given as [25]

$$Z_{s,2} = Z_0 \frac{1 + \Gamma_{s,2}}{1 - \Gamma_{s,2}} \quad \Gamma_{s,2} = S_{22} + \frac{S_{12}S_{21}\Gamma_{s,1}}{1 - S_{11}\Gamma_{s,1}} \quad \Gamma_{s,1} = \frac{Z_{s,1} - Z_0}{Z_{s,1} + Z_0}. \quad (3.4)$$

The following load-pull, or more specifically source-pull, analysis is of a more theoretical nature. Instead of using a discrete set of source impedance values, in

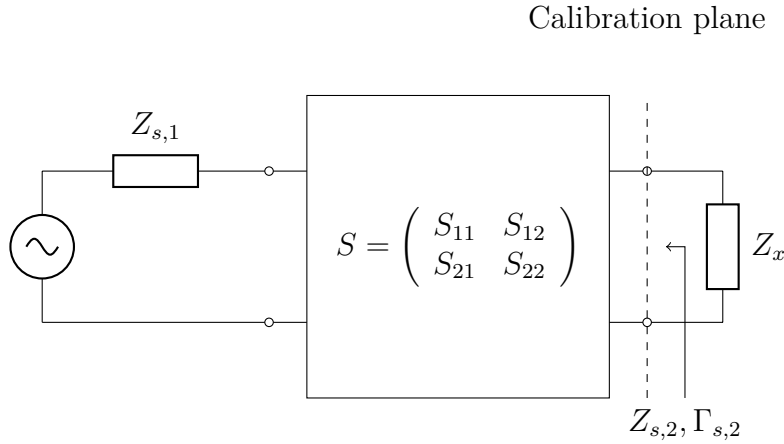


Figure 3.2: Shift of source impedance by means of a two-port transformation.

the measurement of load impedance with a VNA, the source impedance is treated as a continuous variable and measured load impedance is considered as function of delivered power. The mismatch will tell how optimized the power transfer to the transponder is. However, no external optimization for power transfer, by shift of source impedance, is considered, as in the case of transistor source-pull. Performance is rather based on non-linearity impact on mismatch. The arbitrary source impedance is represented by a function average over a certain continuous region in the Smith chart. The key point, and difference to conventional source-pull analysis, is the non-existing knowledge of source impedance. The detailed definitions for this analysis are presented in Section 3.5.

From the RFID perspective, adding a source with free variable impedance puts entirely new conditions on the characterization and performance evaluation of transponders, as compared to the conventional design process of the inlay antenna and transponder RF frontend for the application in far field, or propagating near field. Two environmental facts have been identified: A varying source impedance and non-linearity. What has been established so far is the equivalence between shifted source impedance and mismatch, when referring to the measured impedance as function of delivered power. A straight forward analysis can be performed of how the mismatch factor varies for different source impedances. But is it really this straight forward? The answer is in general, no. A hidden problem is the non-linearity, arriving at the following statement:

The measured impedance at the fundamental frequency, as referenced to a single tone excitation of a non-linear device, depends on the source impedance for any fixed delivered power.

This statement needs some elaboration. To this end consider two cases in measuring the complex impedance of a highly reactive load being in its linear state. This could be done for instance with a linear vector network analyzer (VNA). In the first case let a calibration be done in the standard Z_0 system. In the latter case let a lossless

and reciprocal two-port be inserted, matching the load to 50Ω , and then perform a calibration at the output of the two-port. The situation is illustrated in Figure. 3.3.

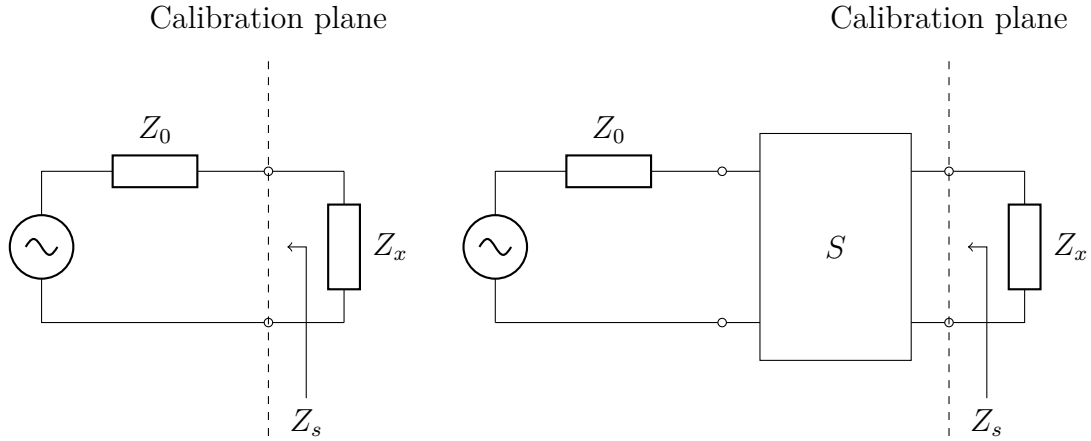


Figure 3.3: Shifted source impedance impact on the measured impedance of a non-linear load.

The calibration at the output of the two-port matching network is not recommended and also not considered in practice. It only serves as a theoretic example. Neglecting any inaccuracies, measurement of the linear state impedance in both cases would yield the same result. However, as soon as the drive level is increased to the non-linear state two different results are obtained, even for the same delivered power. The reason is that the voltage/current time domain solution for the device in the two cases are different, since the source impedance is part of the equation. Or, from a frequency domain perspective harmonics resulting from the non-linearity will add components at the fundamental frequency. Clearly, the equivalent source impedance, as presented at the output of the two-port in the second case, is different (conjugate of device impedance in the linear state) as compared to the first case (Z_0 -system). Consequently, the extracted fundamental Fourier coefficients are different in the two cases, yielding different values of impedance. Note that different complex values of voltage and current can still result in the same delivered power. The fundamental question that comes to mind is what is actually measured.

Note that the phenomena of different measured impedance values in the two cases occurs, despite the fact that calibrations have been carried out. It is concluded from this example, that it is important to know the physical environment that the non-linear device is connected to. Any calibration will not change this environment, since this is a calculated correction yielding correct results for linear devices only. The physical environment, or in other words the presented source impedance, would be obtained by measuring the output impedance of the VNA with for instance another calibrated VNA. Fortunately, the output return loss of a VNA is rather high. Furthermore, any embedding network can be separately characterized. If these conditions are fulfilled, useful results in non-linear characterization may be obtained with a linear VNA, as to the point of knowing what is actually measured. Still the question remains how meaningful measurements of non-linear devices with a linear

VNA can be carried out when the source impedance is considered to be a variable quantity.

As a comparison, in source-pull analysis of a transistor, in general iteration of source impedance is needed for optimized power transfer, and there is also a need of terminations at the harmonic frequencies. In the case of an RFID transponder, the termination at harmonic frequencies is not considered, from a claimed approximation treated in the next section.

3.3 The approximation

After discussing the general behavior of a non-linearity, now consider the restriction where a fixed delivered power yields the same measured impedance, independent of source impedance. The treatment will then be limited to a certain type of devices and cannot be generalized further. In this case the RF frontend of RFID transponders is considered.

Two main observations in the measurement of RFID transponders are discussed in Paper B. These are first the drastic change from a linear state (fixed measured impedance) to the non-linear state (impedance path traced out in the Smith chart) during a sweep of source power. This suggests a close to ideal clipping behavior from a limiter. The subject of ideal strong non-linearity, in the case of transistors, is exploited in literature [26]. Secondly, the measured impedance as function of delivered power remains unchanged when compared for two different source impedances. A further observation is the shift towards a lower real part in the non-linear state, as seen in Figure 3.4.

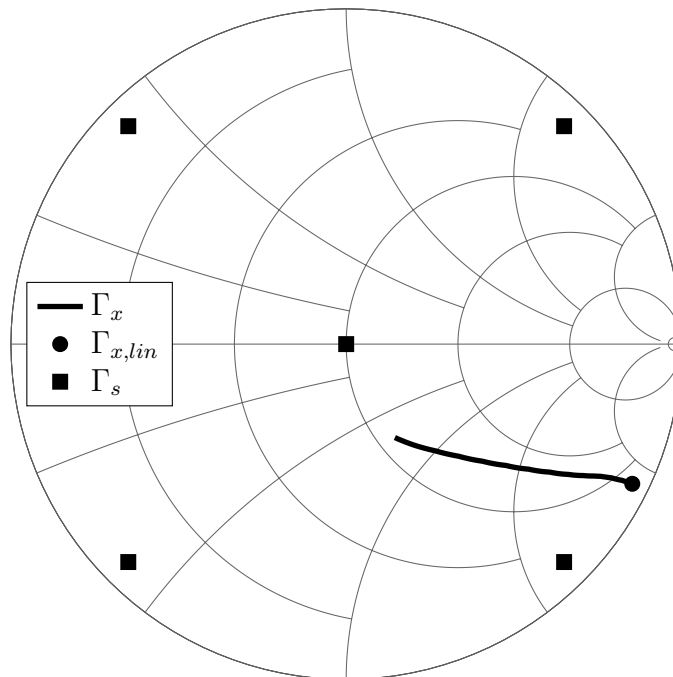


Figure 3.4: An example of the measured impedance for swept source power.

The Smith chart is intuitive in explaining the independency of load impedance on source impedance for fixed delivered power conditions. The square markers in Figure 3.4 indicate different choices of source impedance, some of them towards extreme values. Assume the illustrated non-linear impedance trace, when initially measured in a 50Ω system (center point source impedance). Every point along the trace corresponds to some delivered power. Provided that the available powers of the other source points are adjusted in such way, as to deliver the same delivered power, the claimed approximation will hold when the impedance trace remains unchanged.

3.4 Behavioral model

The shift towards a lower real part in the impedance leaves an interesting circuit topological question: Would it be possible to create a simple circuit model with a behavior mimicking the measured non-linear impedance trace of a transponder? It shall be emphasized that no attempt of rigorous modelling is made here, but rather an as simple as possible circuit description, explaining common behavior among RFID transponder chips. Modeling and design of specific transponder RF frontends is an extensive research topic [14–16,27,28]. The attempt is to only include a resistive non-linearity, whereas any charge function is kept linear. More specifically, the voltage limiter circuit in the transponder, is considered as the representative of the entire non-linearity. Exemplary descriptions of such devices, based on short circuit limitation, are provided in reported work [14, 15].

The linear impedance of the transponder RF frontend is roughly $20 - j200 \Omega$. It turns out that the modeling is topology dependent for capturing the observed behavior. A series RC -circuit topology approaches a pure capacitance after clipping, which would not correctly describe the non-linearity. Left with a parallel topology, consider the circuit shown in Figure 3.5.

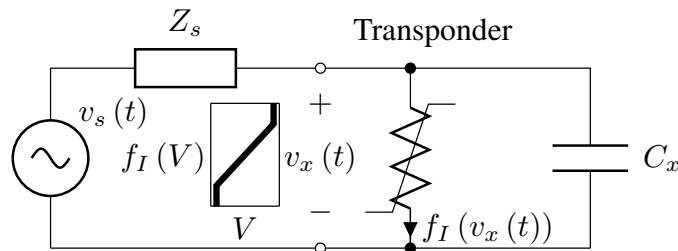


Figure 3.5: A suggested circuit model of non-linear behavior.

The source and reactive part of the transponder are modeled as linear. The shunt non-linearity approaches a short circuit after clipping, which better describes the measured behaviour than a series topology does. Z_s here indicates a general source, which can be of any character, capacitive or inductive, such as for example any of

the points in Figure 3.4. Further assume a voltage/current relationship, given as

$$f_I(V) = \frac{V}{R_x} + \left(\frac{V}{V_{TH}^+} \right)^{2M-1}. \quad (3.5)$$

V_{TH}^+ is the positive clipping threshold. Only symmetrical clipping is considered, i.e., with zero DC component. A single odd order term is chosen since any lower odd order terms would imply stronger non-linearity over the entire range of voltage. This however does not agree with the observation of sudden and distinct clipping. Indeed, as $M \rightarrow \infty$ ideal symmetrical clipping will occur, as plotted in Figure 3.6.

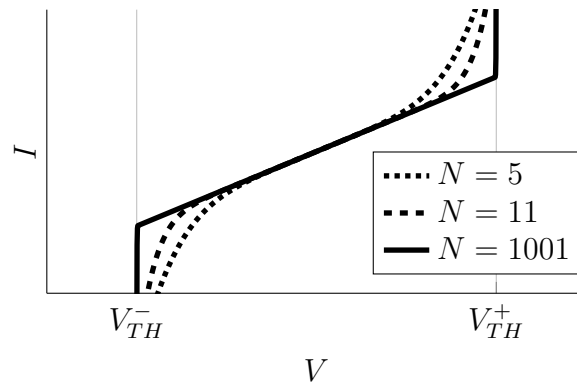


Figure 3.6: Odd order voltage/current relationship with different degrees of non-linearity.

Intuitively, the generation of new frequency components from non-linearity in a device can be understood by looking at the short circuit current, occurring from a sinusoidal voltage source located directly across the device [29]. The short circuit current consists of components at different frequencies, as seen from (3.5). These currents in turn will produce voltages across any other devices, which will act as new voltage sources, and so on. Needless to say, the analysis becomes complex and is only solvable by numerical means and power series reversion techniques [30]. However the following steps can be performed analytically. First denote $N = 2M - 1$, which is an odd integer. Further let the sinusoidal excitation be $v_x(t) = |v_x| \cos \omega_0 t$. Substitution into the odd order term of (3.5) yields

$$\left(\frac{v_x(t)}{V_{TH}^+} \right)^N = \left(\frac{|v_x|}{2V_{TH}^+} \right)^N (e^{j\omega_0 t} + e^{-j\omega_0 t})^N. \quad (3.6)$$

Using the binomial theorem gives [31]

$$\begin{aligned} \left(\frac{v_x(t)}{V_{TH}^+} \right)^N &= \left(\frac{|v_x|}{2V_{TH}^+} \right)^N \sum_{k=0}^N \binom{N}{k} e^{j(N-2k)\omega_0 t} \\ &= \left(\frac{|v_x|}{2V_{TH}^+} \right)^N \sum_{k=0}^N \frac{N!}{k!(N-k)!} e^{j(N-2k)\omega_0 t}. \end{aligned} \quad (3.7)$$

From this expression it is also seen that since $N - 2k$ is always odd, only odd harmonics are generated. The contribution at the l :th harmonic will be constrained by the condition $N - 2k = \pm l$ from which

$$\begin{aligned} \left(\frac{v_x(t)}{V_{TH}^+} \right)_{l\omega_0}^N &= \left(\frac{|v_x|}{2V_{TH}^+} \right)^N \times \\ &\left(\frac{N!}{\left(\frac{N-l}{2}\right)! \left(\frac{N+l}{2}\right)!} e^{jl\omega_0 t} + \frac{N!}{\left(\frac{N+l}{2}\right)! \left(\frac{N-l}{2}\right)!} e^{-jl\omega_0 t} \right) \\ &= \left(\frac{|v_x|}{V_{TH}^+} \right)^N \frac{2^{N+1}}{(N-l)! \prod_{m=1}^l (N+m)} \cos l\omega_0 t. \end{aligned} \quad (3.8)$$

Since the numerator is of the form $a^N 2^{N+1}$ and the denominator always has N factors where $N - l > 2$ for sufficiently large N and increasing, the contribution will approach zero as $N \rightarrow \infty$. However, then f_I approaches the non differentiable ideal clipping state. In time domain this state can be regarded as a short circuit voltage in the waveform, being equivalent to an ideal diode characteristic, with the difference that conduction occurs in both directions for positive and negative half periods.

Analogous to the established theory on reduced conduction angle analysis for high efficiency power amplifiers, a reduced “voltage” angle analysis can be done for the described behavior of RFID transponders [26]. Provided the waveform is analytic, Fourier analysis can be used as a tool. Consider again the ideal resistive non-linearity in (3.5) when $M \rightarrow \infty$. From the discussion the waveforms with the substitution $\theta = \omega_0 t$ are as illustrated in Figure 3.7.

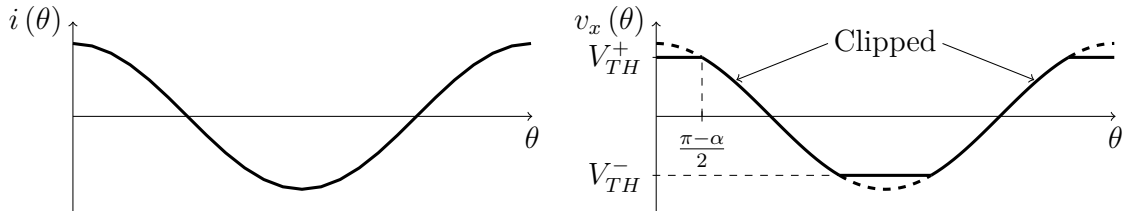


Figure 3.7: Waveforms of an ideal voltage clipping characteristic.

The definition of the clipped v is

$$v_x(\theta) = \begin{cases} V_{TH}^+, & \theta \in \left[-\frac{\pi-\alpha}{2}, \frac{\pi-\alpha}{2}\right] \\ |v_x| \cos \theta, & \theta \in \left[-\frac{\pi+\alpha}{2}, -\frac{\pi-\alpha}{2}\right], \theta \in \left[\frac{\pi-\alpha}{2}, \frac{\pi+\alpha}{2}\right] \\ V_{TH}^-, & \theta \in \left[-\pi, -\frac{\pi-\alpha}{2}\right], \theta \in \left[\frac{\pi+\alpha}{2}, \pi\right]. \end{cases} \quad (3.9)$$

The k :th harmonic of a general periodic function $f(t)$ is given as the Fourier coefficients

$$F_k = \frac{1}{\pi} \int_{-\pi}^{\pi} f\left(\frac{\theta}{\omega}\right) \cos(k\theta) d\theta. \quad (3.10)$$

Substitution of (3.9) into (3.10) for the five intervals yields

$$\begin{aligned}
V_{x,k} = & \frac{V_{TH}^+}{\pi} \int_{-\frac{\pi-\alpha}{2}}^{\frac{\pi-\alpha}{2}} \cos(k\theta) d\theta + \frac{V_{TH}^-}{\pi} \int_{-\pi}^{-\frac{\pi+\alpha}{2}} \cos(k\theta) d\theta + \frac{V_{TH}^-}{\pi} \int_{\frac{\pi+\alpha}{2}}^{\pi} \cos(k\theta) d\theta \\
& + \frac{|v_x|}{\pi} \int_{-\frac{\pi-\alpha}{2}}^{\frac{\pi-\alpha}{2}} \cos\theta \cos(k\theta) d\theta + \frac{|v_x|}{\pi} \int_{\frac{\pi+\alpha}{2}}^{\pi} \cos\theta \cos(k\theta) d\theta.
\end{aligned} \tag{3.11}$$

These are standard integrals and after some manipulation, with $V_{TH}^- = -V_{TH}^+$ from symmetrical clipping, the fundamental and k :th harmonic are respectively given as

$$V_{x,1} = \frac{4V_{TH}^+}{\pi} \cos\left(\frac{\alpha}{2}\right) + \frac{|v_x|}{2\pi} (2\alpha - \sin\alpha) \tag{3.12}$$

$$\begin{aligned}
V_{x,k} = & \frac{4V_{TH}^+}{k\pi} \cos\left(\frac{\alpha}{2}\right) + \frac{|v_x|}{\pi} \left(\frac{\sin\left(\frac{(k+1)(\pi+\alpha)}{2}\right)}{k+1} + \frac{\sin\left(\frac{(k-1)(\pi+\alpha)}{2}\right)}{k-1} \right. \\
& \left. - \frac{\sin\left(\frac{(k+1)(\pi-\alpha)}{2}\right)}{k+1} - \frac{\sin\left(\frac{(k-1)(\pi-\alpha)}{2}\right)}{k-1} \right), \quad k = 3, 5, 7, \dots
\end{aligned} \tag{3.13}$$

Consider now the fundamental (3.12). The voltage angle α is an indication of the drive level from the source. It was concluded that the short circuit harmonic current generation approaches zero for the ideal f_I in (3.8). For the more realistic circuit in Figure 3.5, the resistor voltage amplitude at the entry level of non-linear state would be equivalent with the short circuit case, and can be written

$$|v_x| = |V_{x,1}| = \frac{|v_s|}{\left|1 + \frac{Z_s}{R_x} + j\omega_0 Z_s C_x\right|}. \tag{3.14}$$

It is not clear what happens when the source voltage is increased into the non-linear state, since this is only solvable by numerical means, like, e.g., a harmonic balance method [29]. Yet still, in the short circuit case (3.12) is bounded, since any increase in $|v_x|$ will yield a decrease in α . It is also seen numerically from simulations for the circuit in Figure 3.5 that the amplitude of the resistor voltage at the fundamental remains approximately constant in the clipped region. Consequently, if the delivered power is fixed, from the topology it is seen that the real part of admittance will also be fixed. The overall conclusion is that the in-band distortion has limited impact on the transponder impedance at the fundamental frequency.

3.5 Figure of merit calculation

After the discussion in Sections 3.2-3.3 the central assumption arrived at is:

The measured impedance at the fundamental frequency, for a fixed delivered power, is independent of the source impedance.

Based on this assumption, in Paper B mismatch theory is used to provide a tool set, from which a FOM can be derived. The theory is developed in the next subsections.

3.5.1 Mismatch theory for source impedance shift

The delivered power to the transponder is given as

$$P_{xL} = MP_{AVS} = \frac{4R_s R_{xL}}{|Z_s + Z_{xL}|^2} P_{AVS} = \frac{(1 - |\Gamma_s|^2)(1 - |\Gamma_{xL}|^2)}{|1 - \Gamma_s \Gamma_{xL}|^2} P_{AVS} \quad (3.15)$$

where (3.1) is used, which is expressed in terms of reflection coefficients [25]. Here Γ_s and Γ_{xL} are the source and transponder reflection coefficients, respectively. The conversion between impedance and reflection coefficient is

$$\Gamma_s = \frac{Z_s - Z_0}{Z_s + Z_0} \quad \Gamma_{xL} = \frac{Z_{xL} - Z_0}{Z_{xL} + Z_0}. \quad (3.16)$$

The index L has been added since in general the pulsed low state impedance is considered. The modulation and RFID protocol were described in Appendix A.

Consider now the mismatch in (3.15), as referred to the Γ_s -plane, where M is a constant. The expression for M can be rearranged into the equation for a circle in the Γ_s -plane for constant M , see B.1 in Appendix B. The Γ_s -values yielding a constant mismatch factor M for a fixed Γ_{xL} are found on a circle with center C_M and radius r_M , respectively given as

$$C_M = \frac{M\Gamma_{xL}^*}{1 - (1 - M)|\Gamma_{xL}|^2}, r_M = \frac{\sqrt{1 - M}(1 - |\Gamma_{xL}|^2)}{1 - (1 - M)|\Gamma_{xL}|^2}. \quad (3.17)$$

The terms impedance and reflection coefficients will be used interchangeably for Γ and Z , respectively.

The power swept non-linear impedance path, as discussed in Section 3.3, is now complemented with its conjugate for reference to source impedance, shown in Figure 3.8.

The power sweep starts at threshold of backscatter modulation ($\Gamma_{xL,th}^*$, $P_{xL,th}$), indicated by the circle marker located at the outer rim of the Smith chart. An offset point ($\Gamma_{xL,offset}^*$, $P_{xL,offset}$) along the power sweep is indicated by the square marker. Note that since a non-linearity is considered the impedance is only valid for a certain delivered power, therefore mentioned explicitly. Further an arbitrarily chosen source impedance, denoted Γ_s , is indicated by the asterisk.

Let $\{M, \Gamma_{xL}\}$ in (3.17) be replaced by $\{M_{L,th}, \Gamma_{xL,th}\}$ and $\{M_{L,offset}, \Gamma_{xL,offset}\}$, respectively representing the threshold and offset case. The corresponding mismatch circles are also plotted in Figure 3.8. The solid circle illustrates the mismatch between source Γ_s and load $\Gamma_{xL,th}$. The dashed circle illustrates the mismatch between source Γ_s and load $\Gamma_{xL,offset}$. It is clear that the mismatch values generally are different in the two cases. For a linear load these two circles would align.

The mismatch quotient, denoted k_M , is defined as

$$k_M \equiv \frac{M_{L,offset}}{M_{L,th}} = \frac{(1 - |\Gamma_{xL,offset}|^2) |1 - \Gamma_s \Gamma_{xL,th}|^2}{(1 - |\Gamma_{xL,th}|^2) |1 - \Gamma_s \Gamma_{xL,offset}|^2}. \quad (3.18)$$

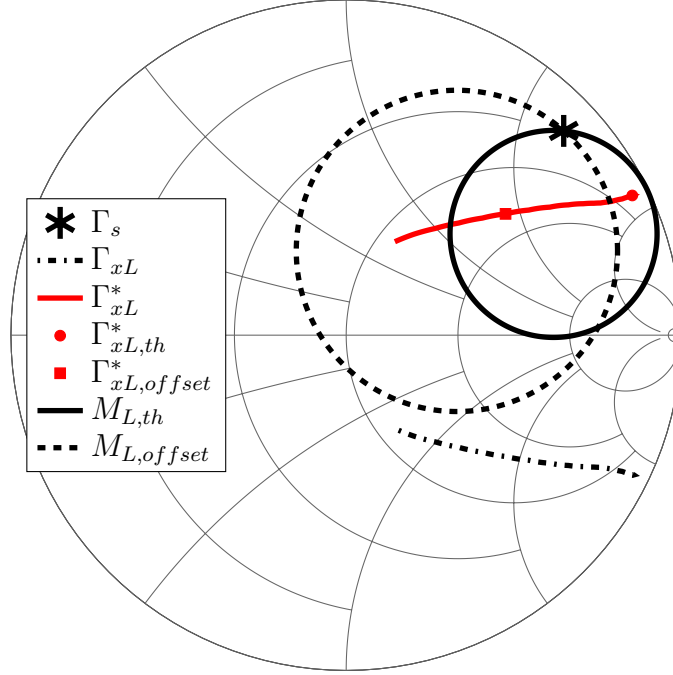


Figure 3.8: Mismatch circles for a non-linear load excited by a source (asterisk). Solid circle: Threshold mismatch. Dashed circle: Offset mismatch.

It indicates the non-linear impact on the available power ratio between threshold and offset state. For a linear load $k_M = 1$. k_M will be bounded when $|\Gamma_{xL,th}| < 1$, $|\Gamma_{xL,offset}| < 1$ and $|\Gamma_s| \leq 1$.

Depending on where in the Smith chart the source is located k_M can have values both below and above unity for a non-linear load. If k_M is constrained to unity, manipulation of (3.18) yields

$$\left| \frac{\Gamma_{xL,th}\Gamma_s - 1}{\Gamma_{xL,offset}\Gamma_s - 1} \right| = \sqrt{\frac{1 - |\Gamma_{xL,th}|^2}{1 - |\Gamma_{xL,offset}|^2}} \quad (3.19)$$

which is recognized as a bilinear mapping yielding a circle in the Γ_s -plane, as shown dashed in Fig. 3.9.

Using the notations in Appendix B, the center and radius are given as

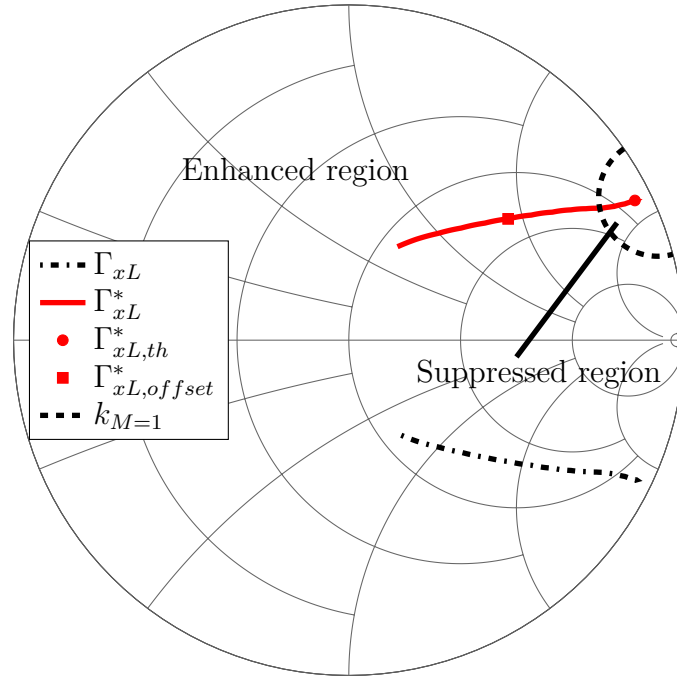
$$C_{k_M=1} = \frac{\alpha^2 c^* d - a^* b}{|a|^2 - \alpha^2 |c|^2} \quad r_{k_M=1} = \frac{\alpha |ad - bc|}{\left| |a|^2 - \alpha^2 |c|^2 \right|} \quad (3.20)$$

where the terms are identified as

$$a = \Gamma_{xL,th} \quad b = -1 \quad c = \Gamma_{xL,offset} \quad d = -1$$

$$\alpha = \sqrt{\frac{1 - |\Gamma_{xL,th}|^2}{1 - |\Gamma_{xL,offset}|^2}}. \quad (3.21)$$

The circle boundary will divide the Smith chart into two distinct regions, where Γ_s can reside. The region where $k_M < 1$ will be called the suppressed region, denoted

Figure 3.9: Unity mismatch quotient circle ($k_M = 1$).

Ω_s . In Ω_s the mismatch condition yields a non-linear growth of available power for increased delivered power, as compared to the linear case. Correspondingly the region where $k_M > 1$ will be called the enhanced region, denoted Ω_e . In Ω_e the non-linearity yields a reduction in needed offset available power for increased delivered power, as compared to the linear case. In other words the load is pushed towards a better mismatch condition.

3.5.2 The $|\Delta\Gamma|$ -value

The mismatch theory developed in the previous section is suitable for measured data taken from a linear VNA. One more quantity, needed for the definition of FOM, is the $|\Delta\Gamma|$ -value. The communication between the transponder is half duplex, meaning that the broadcast from the interrogator is followed by a reply from the targeted transponder, in that particular order. The communication can never occur simultaneously (full duplex). The response from the transponder is based on modulation of the input impedance at the RF frontend. The modulation consists of the shift between two distinct values, low and high state. The low state is equivalent to the absorbing or scavenging mode. The high state is basically a drastic shift of the impedance imaginary part. An example of the pulsed impedance, measured by the VNA in pulse profile mode, is shown in Figure 3.10.

Based on the pulsed impedance data, the magnitude of the difference in reflection coefficient between high and low state can be calculated. Accordingly it is defined

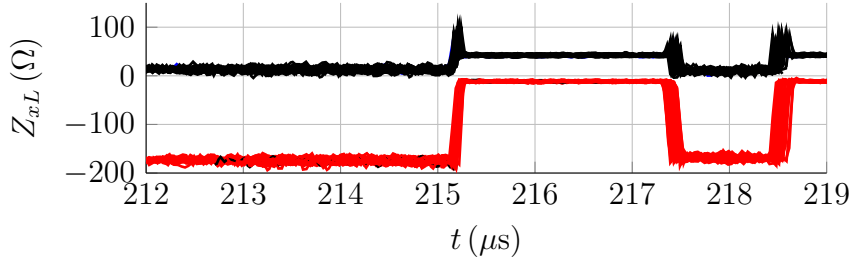


Figure 3.10: Overlaid sweep samples of the pulsed impedance, as measured by the VNA.

as [32]

$$|\Delta\Gamma| \equiv \left| \frac{Z_{xH} - Z_s^*}{Z_{xH} + Z_s} - \frac{Z_{xL} - Z_s^*}{Z_{xL} + Z_s} \right|. \quad (3.22)$$

The $|\Delta\Gamma|$ -value is bounded for all possible values of source impedance, with a maximum value of $|\Delta\Gamma| = 2$ when the state switches between 0 and ∞ . This is very important for the definition of FOM.

3.5.3 Figure of merit

The quantities for the definition of FOM have been derived. These are the mismatch quotient k_M from (3.18) and the $|\Delta\Gamma|$ -value from (3.22). Clearly, both these quantities, depend on the source impedance and are well defined functions over the entire Smith chart. The idea is now to define a FOM-function operating on the Smith chart, comparing the threshold state with the offset state. From the previous mismatch theory it was concluded that the suppressed region, defined by the unity mismatch quotient condition, contains the source impedance values where the mismatch condition yields a non-linear growth of available power for increased delivered power, as compared to the linear case. For stronger non-linearities k_M increases.

An increase in the $|\Delta\Gamma|$ -value yields a higher quality in backscatter response from the transponder. Taking both the threshold and offset value into account, the obvious choice would be to take the product. The quotient, for instance $|\Delta\Gamma_{offset}/\Delta\Gamma_{th}|^2$, would be undefined for $|\Delta\Gamma| = 0$, which is true if $Z_{xL} \approx Z_{xH}$, or $Z_s \rightarrow \infty$.

The FOM function is now composed as

$$f_{FOM}(\Delta P, r, \varphi) = |\Delta\Gamma_{th}(\Delta P, r, \varphi) \Delta\Gamma_{offset}(\Delta P, r, \varphi)|^2 k_M(\Delta P, r, \varphi) \quad (3.23)$$

where $P_{xL,offset} = P_{xL,th} + \Delta P$. (r, φ) are the polar coordinates, i.e., $\Gamma_s = r e^{j\varphi}$. f_{FOM} expresses an estimate on offset flexibility, i.e., the strength of non-linearity, weighted by the strength of backscatter modulation. Different alternatives are possible for comparison, by setting one or several of the quantities $\Delta\Gamma_{th}$, $\Delta\Gamma_{offset}$ or k_M to unity. Only the suppressed region (Ω_s) is considered, where an increased value of both k_M and $|\Delta\Gamma|$ indicates a better performance.

For an estimate on the entire region, the final FOM is calculated as the function average according to

$$I_{FOM}(\Delta P) = \frac{1}{A} \int_{\varphi_1}^{\varphi_2} \int_{r_1}^1 f_{FOM}(\Delta P, r, \varphi) r dr d\varphi \quad (3.24)$$

where A is the area of the region of integration. Since f_{FOM} is bounded on the entire region of integration it is valid. The boundary of integration is given by the intersection between the unity mismatch quotient circle (3.20) and the Smith chart. Denote the intersection points $z_{is1,2} = (x \mp jy) e^{j \arg(C_{k_M=1})}$, which from the circle definition give the set of equations

$$\begin{aligned} x^2 + y^2 &= 1 \\ (x - |C_{k_M=1}|)^2 + y^2 &= r_{k_M=1}^2. \end{aligned} \quad (3.25)$$

Manipulation and solving for (x, y) yields

$$\begin{aligned} z_{is1,2} &= \left(\frac{|C_{k_M=1}|^2 - r_{k_M=1}^2 + 1}{2|C_{k_M=1}|} \right. \\ &\quad \left. \mp j \frac{\sqrt{4|C_{k_M=1}|^2 - (|C_{k_M=1}|^2 - r_{k_M=1}^2 + 1)^2}}{2|C_{k_M=1}|} \right) \\ &\quad \times e^{j \arg(C_{k_M=1})} \end{aligned} \quad (3.26)$$

where the boundary is given by

$$\begin{aligned} \varphi_1 &= \arg z_{is1} \leq \varphi \leq \arg z_{is2} = \varphi_2 \\ r_1 &= |C_{k_M=1} + r_{k_M=1} e^{j\theta}| \leq r \leq 1 \\ \theta &= \pi + \varphi + \arcsin \left(\frac{|C_{k_M=1}|}{r_{k_M=1}} \sin(\arg(C_{k_M=1}) - \varphi) \right). \end{aligned} \quad (3.27)$$

In summary the described procedure will give an estimate on mismatch roughness under a changed source environment from the conjugate state, when the delivered power needs to be adjusted to a higher value. In other words the FOM will tell how flexible the transponder response is to a shifted source impedance. It also takes into account how the backscatter modulation is affected by including the $|\Delta\Gamma|$ -value.

The offset point may represent a state of higher delivered power where some added functionality in the transponder is needed. The adjustment to higher delivered power is in particular common when writing to the transponder memory as compared to only reading from it. The memory in the transponder needs higher power levels for writing. This is a critical measure in RNF RFID, with an altered RNF surrounding the RFID tag.

3.6 Measurement system

The core implementation of the measurement system is the mimicking of the RFID wake-up signal, as described in Section A.2, combined with the electrical measurement of complex impedance within a pulse of the back scattered reply from the transponder. The realization of such a setup may be done in many different ways. One alternative is to use a vector signal generator with the VNA and external pulse modulators, which are directly connected to the VNA [11].

After inventory of the different possibilities it was found that the many options available in instruments provided by Rohde & Schwarz[®] (R&S) would enable a compact setup, consisting of only two instruments [33]. These are the ZVA (VNA) and ZVAX extension unit (EU). The big memory available for long recording times enables the entire wake-up signal to be generated as one single pulse profile, including the back scatter response from the transponder. A graphical user interface (GUI), see Appendix C, is programmed for communication between the instruments and MATLAB on the PC host, by means of SCPI commands over a GPIB connection [34]. Virtually all commands controlling the instruments are accessible. When the ZVA and ZVAX are connected together they present a common programming interface towards MATLAB.

3.6.1 Setup

A bench diagram of the complete setup is shown in Figure 3.11. The device under test (DUT) connection methods are described in Chapter 2. The purpose of the EU is to add extra components into the RF path. This is possible from the direct access at the VNA ports. The EU contains several paths, with harmonic filters, pulse modulators and combiners. The application in Paper B only uses the pulse modulator for one port. The possibility of differential pulse modulation was investigated, but unsuccessful to implement. However, for unmodulated measurements of transponder impedance the true differential mode (TDM) option in the VNA was used.

Tuners from Maury Microwave are inserted between the VNA ports and the probe connection, in order to shift the source impedance presented towards the transponder [35].

In summary the setup enables the following measurement combinations:

- Single ended (one-port) unmodulated impedance without source shift
- Differential (two-port) unmodulated impedance without source shift
- Single ended (one-port) unmodulated impedance with source shift
- Differential (two-port) unmodulated impedance with source shift
- Single ended (one-port) modulated impedance without source shift
- Single ended (one-port) modulated impedance with source shift

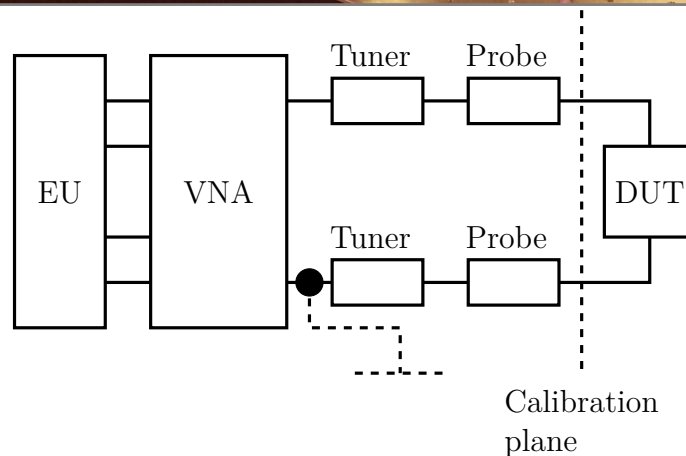
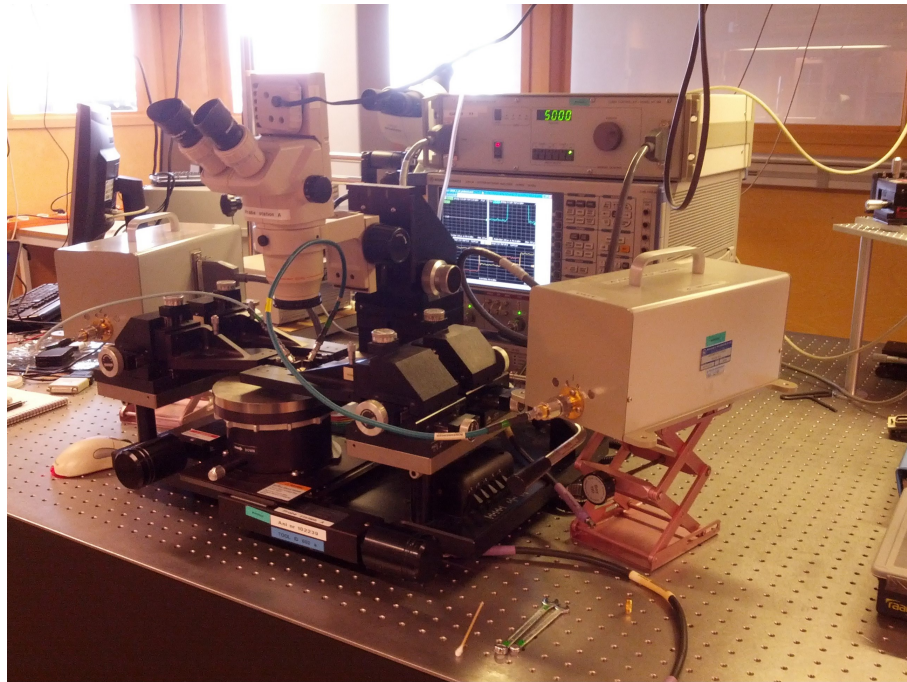


Figure 3.11: Top: Measurement system including ZVA24, ZVAX, probe station, and tuners with control box. Bottom: Bench diagram. The calibration plane is valid when the tuners are set to $50\ \Omega$ only. For source shift pre-characterization with de-embedding is done.

Despite the possibilities listed the source shift in Paper B is done single ended for an approximate conjugate match of the transponder RF frontend, which is highly reactive. This was accomplished by short circuiting one of the tuners, which is indicated by the dashed ground connection in Figure 3.11.

The frequency characteristics of the transponder chip are rather broadband over the UHF RFID band [2] and the same pulsed behaviour is expected across the band so a modulation frequency in the middle of the band at 915 MHz is chosen. This frequency was also chosen for the matched measurement. A frequency sweep is only performed for the unmodulated unmatched condition in TDM.

3.6.2 Device under test

The transponder chips characterized in Paper B are from different vendors with several individuals of each. For the purpose of stable measurements a more robust extension to the probe connections discussed in Section 2.1 is fabricated. Figure 3.12 shows a substrate with a 6 chip type by 5 individual array of pads. The chip types are labeled Type A to Type F. Each pad consists of a quadratic ground plane with a milled hole in the middle. The holes have diameters providing some margin to the chip dimensions, which roughly vary from 700 to 900 microns in diameter. They are milled to an approximate depth corresponding to the wafer thicknesses, which vary from 70 to 150 microns. As was explained in Section 2.2 flexibility of the probe tips was needed.

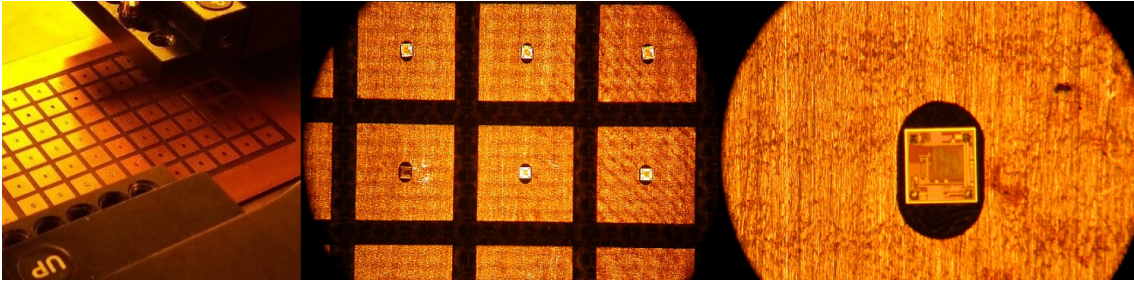


Figure 3.12: Substrate with seven-by-ten transponder chip array of which 6×5 is used.

From the discussion in Section 2.2 the flexibility of the probe in combination with the loose placement of the chips proved to work well for the electrical connection. The dual probe connection is used consistently for all measurements. Note that the unmatched single ended and differential methods both provide a 100Ω source impedance from the two port topology shown in Figure 3.13.

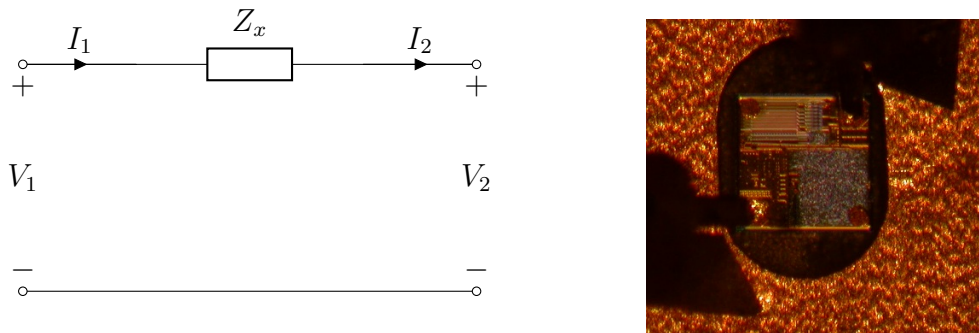


Figure 3.13: Left: General topology for DUT. Right: Dual probe connection.

3.6.3 Matched condition

In the matched condition one of the tuners is short circuited for high reactance. The purpose of the matched compared to the unmatched conditions is to create two distinct source impedances for the verification of source independency of measured impedance as function of delivered power, as discussed in Sections 3.3-3.4. With the DUT connected the tuner is adjusted for an approximate match. Note that the tuning is done at low power, i.e., in the linear state. Since all transponder types have linear impedances in the same range, the tuner setting can be kept fixed for all DUTs.

According to Figure 3.14 the source match Z_{sm} is a series impedance and in this case the de-embedding is calculated as $Z_x = Z_m - Z_{sm}$, where Z_m is the measured impedance in the calibration plane.

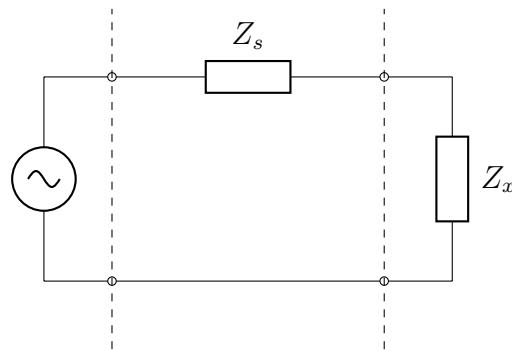


Figure 3.14: Source match configured as two port topology.

During pre-characterization, due to the simple topology, a one-port measurement of the source match is performed. The source impedance at 915 MHz is evaluated to $92 + j164 \Omega$.

3.7 Verification of repeatability

A starting point for the measurements are repeatability over individuals. From the transponder types measured Type A - C are from the same vendor, but of different versions. The same holds for Type D and Type E. Tabled data of the maximum variance over individuals for each type over the power sweep is summarized in Table 3.1 and Table 3.2, for unmatched and matched conditions, respectively.

It is concluded that the maximum variance occurs at low power levels for the reactance for Type D, where the reactance has its maximum value. Hence, it does not have a big impact on the averaging. Comparably low values of variance are seen for the remaining transponder types.

Table 3.1: Maximum unmatched variance in sample repeatability.
Re: Real Part. Im: Imaginary Part.

Type	$\max(\text{Var}(Z_{xL}))$ (Ω^2)	P_{xL} (dBm)	$P_{xL,min}$ (dBm)	$P_{xL,max}$ (dBm)
A	8 (Re)	-1	-21	10
B	5 (Im)	-26	-27	10
C	5 (Im)	-18	-28	10
D	19 (Im)	-27	-28	8
E	19 (Im)	-18	-34	9
F	2 (Im)	-33	-33	8

Table 3.2: Maximum matched variance in sample repeatability.
Re: Real Part. Im: Imaginary Part.

Type	$\max(\text{Var}(Z_{xL}))$ (Ω^2)	P_{xL} (dBm)	$P_{xL,min}$ (dBm)	$P_{xL,max}$ (dBm)
A	18 (Re)	-2	-21	10
B	6 (Im)	-4	-27	10
C	3 (Im)	-25	-28	10
D	31 (Im)	-25	-28	8
E	18 (Im)	-16	-34	9
F	4 (Im)	8	-33	8

3.8 Verification of source independency

An important measurement is the verification that the transponder impedance for a fixed delivered power is independent of the source impedance, which is a necessary requirement for the FOM analysis to hold. Two distinct source impedances are chosen for this task. It shall be emphasized that the approximation is based on only two distinct values of source impedance, the unmatched 100 Ω system and the close to conjugate match, see Section 3.6.3. Today, no measured knowledge based on a larger set of source impedances exists. The theoretical treatment of an arbitrary source impedance in Sections 3.2-3.4 is less straight forward, so a general investigation is a rather complex subject.

In the verification method the delivered power is calculated from knowledge of the source impedance. Data is taken from the power swept impedance measurement at low impedance state. The results will partly tell how the unmatched to matched condition deviation develops along delivered power, partly give information on the individual variation. A summary of maximum unmatched to matched impedance deviation and variance is given in Table 3.3 and Table 3.4, respectively.

Table 3.3: Maximum unmatched to unmatched impedance deviation.
Re: Real Part. Im: Imaginary Part.

Type	$\max(\Delta(Z_{xL}))$ (Ω)	P_{xL} (dBm)	$P_{xL,min}$ (dBm)	$P_{xL,max}$ (dBm)
A	12 (Im)	10	-21	10
B	-11 (Im)	10	-27	10
C	-13 (Im)	-14	-28	10
D	-15 (Im)	-5	-28	8
E	15 (Re)	7	-34	9
F	-23 (Im)	8	-33	8

Table 3.4: Maximum unmatched to matched impedance variance.
Re: Real Part. Im: Imaginary Part.

Type	$\max(Var(Z_{xL}))$ (Ω^2)	P_{xL} (dBm)	$P_{xL,min}$ (dBm)	$P_{xL,max}$ (dBm)
A	42 (Re)	-2	-21	10
B	2 (Re)	10	-27	10
C	5 (Im)	-19	-28	10
D	25 (Im)	-25	-28	8
E	50 (Im)	-16	-34	9
F	5 (Im)	-31	-33	8

A general expectation is that the approximation of impedance independency on delivered power loses validity for high power levels. The highest impedance deviation is seen for Type F and the same behaviour is also seen for Type A, B and E from the values in Table 3.3. No particular trend could be seen over delivered power for Type C and Type D. Power swept data for Type C and F are plotted for comparison in Figures 3.15 and 3.16, respectively. For deviation between unmatched and matched state along power, the left hand plots are considered. For individual variation, the right hands plots are considered. Further information on power swept data for the remaining types are found in Paper B.

Generally, the levels within the first 10 dB after transponder activation are considered to be within acceptable limits for all types. This is about -20 to -15 dBm of delivered power, depending on transponder type. Relatively speaking, for Type C and Type D, the deviation is small in imaginary part, since the reactance has its highest values in this power interval.

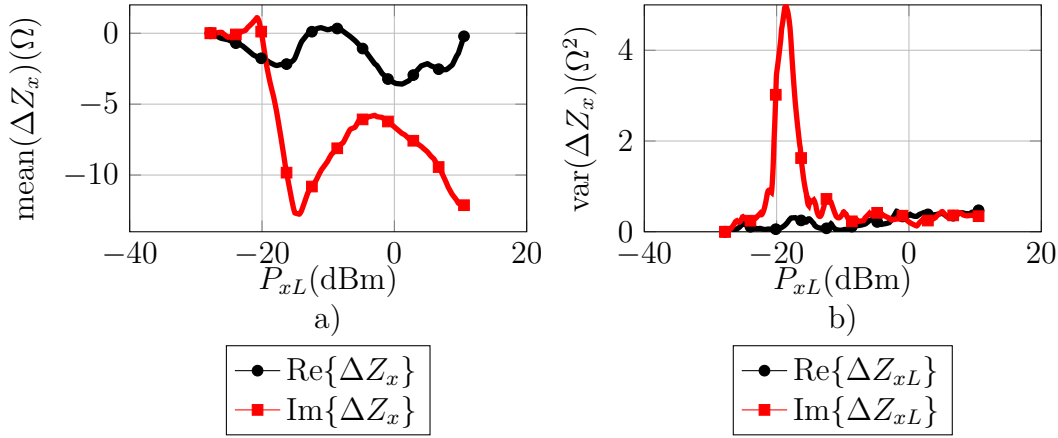


Figure 3.15: Source shift impact Type C. $Z_S = 100 \Omega$ and $Z_S = 92 + j164 \Omega$.
a) Mean deviation. b) Variance.

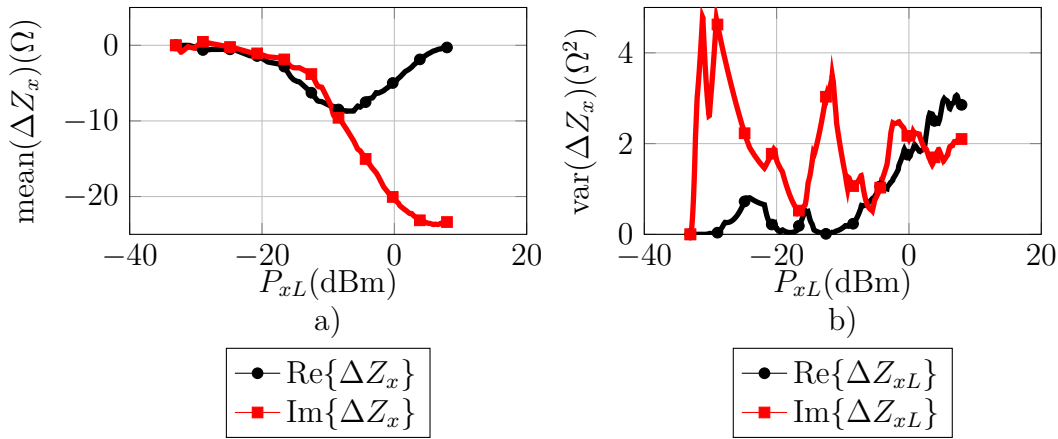


Figure 3.16: Source shift impact Type F. $Z_S = 100 \Omega$ and $Z_S = 92 + j164 \Omega$.
a) Mean deviation. b) Variance.

From a real life testing perspective rather the low end of the power interval, above threshold of activation, is of interest. The conclusion is that the approximation of source impedance independency holds. It is also concluded that averaging will give a good representative for the calculation of FOM, treated in the next section.

3.9 Post analysis

The verification of repeatability and source independency in Sections 3.7 and 3.8 is done over individuals. For the FOM calculations treated next an average over individuals is chosen as the representative for each type on the pulsed data. It is explained in Appendix A.3 that the commands included in the VNA pulse profile and backscatter response from the transponder define a single sweep. The wake up sequence and time window for response detection is cycled periodically. Since the delay between trigger and response is random for each sweep, a post processing

of the data is required to enable averaging. It basically consists of adding time offsets to the backscatter response sweeps, illustrated in Figure 3.17. After sorting an average can be calculated for the low and high pulse state. High state is defined as the high value of the imaginary part (negative values), i.e., after the switch from the absorbing state (low state) to a close to zero value. A sorting algorithm has been implemented and available as one of the features in the post analysis GUI. The algorithm is described in the Appendix C.

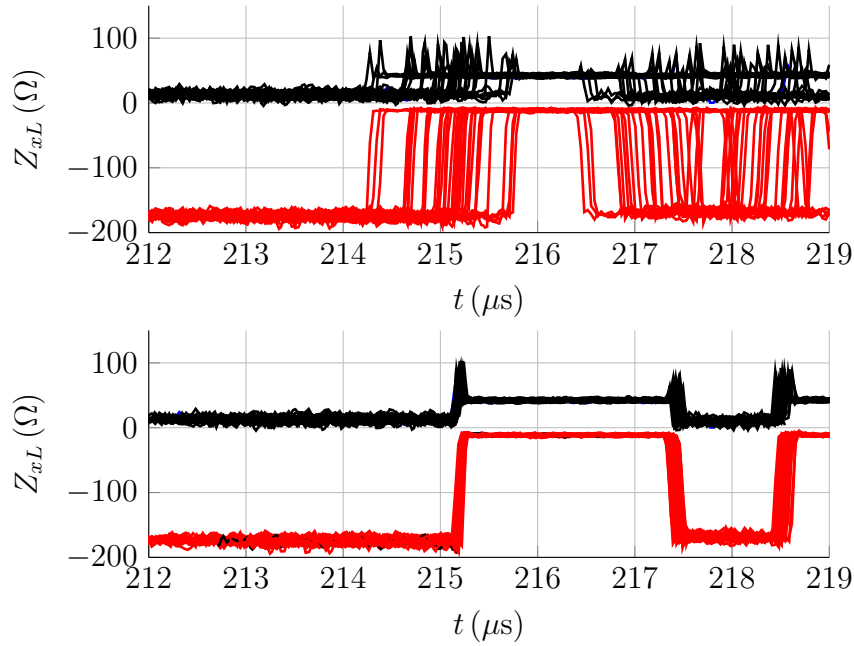


Figure 3.17: Sweep and sample sorting of pulse profile. Top: Before sorting. Bottom: After sorting. Impedance real and imaginary parts are distinguished being strictly positive and negative, respectively.

3.10 Measured FOM

In the calculation of FOM both the $|\Delta\Gamma|$ -value and mismatch quotient k_M , as defined in Section 3.5.3, are taken into account. The power sweep consists of an offset of delivered power from the threshold of response. The $|\Delta\Gamma|$ -value and k_M are first treated separately and then combined for the final FOM. Initially, the $|\Delta\Gamma|$ -value is calculated over swept offset of delivered power, when the source impedance is fixed to a conjugate of the measured impedance at threshold ($\Gamma_{xL,th}^*$), shown in Figure 3.18.

Figure 3.18 represents the far field case, with an antenna conjugately matched to the transponder. This situation is not commonly found inside an RFID printer, but the results give useful information of the performance in an RFID system. From the results Type A supersedes the remaining types, where Type D, an older chip version has the lowest maximum, i.e., in the vicinity of threshold response. The remaining types show similar performance.

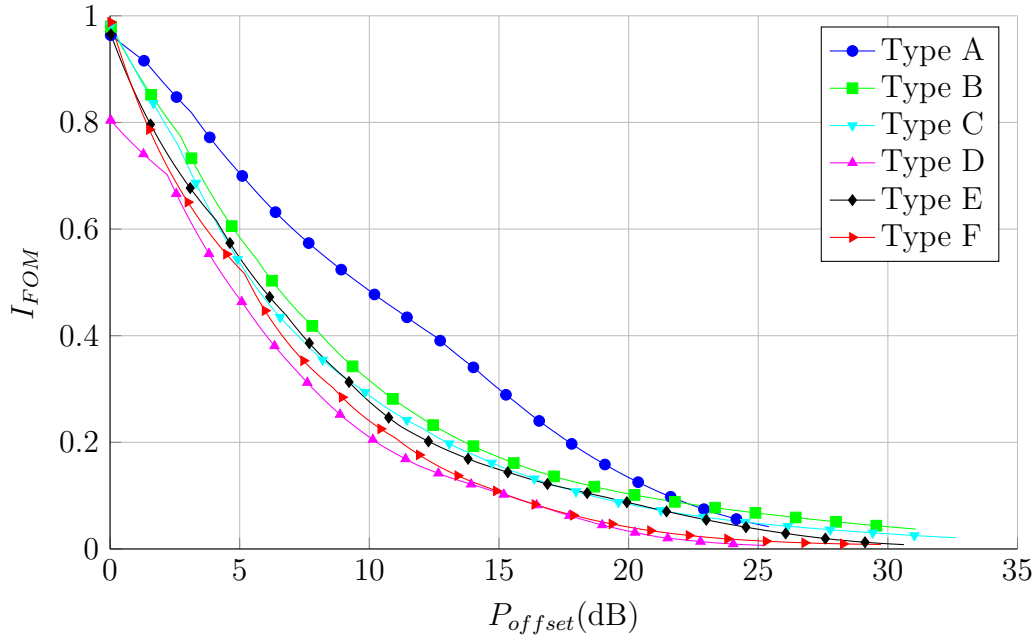


Figure 3.18: Power sweep of $|\Delta\Gamma|$ for fixed source impedance $\Gamma_s = \Gamma_{xL,th}^*$.

Next the $|\Delta\Gamma|$ -value is considered as function average over the suppressed region, with $f_{FOM} = |\Delta\Gamma_{offset}|$ and $k_M = |\Delta\Gamma_{offset}| = 1$ in (3.23). This case represents the situation when the source Γ_s is located anywhere in the suppressed regions, as compared to the fixed case illustrated in Figure 3.18. It is plotted in Figure 3.19.

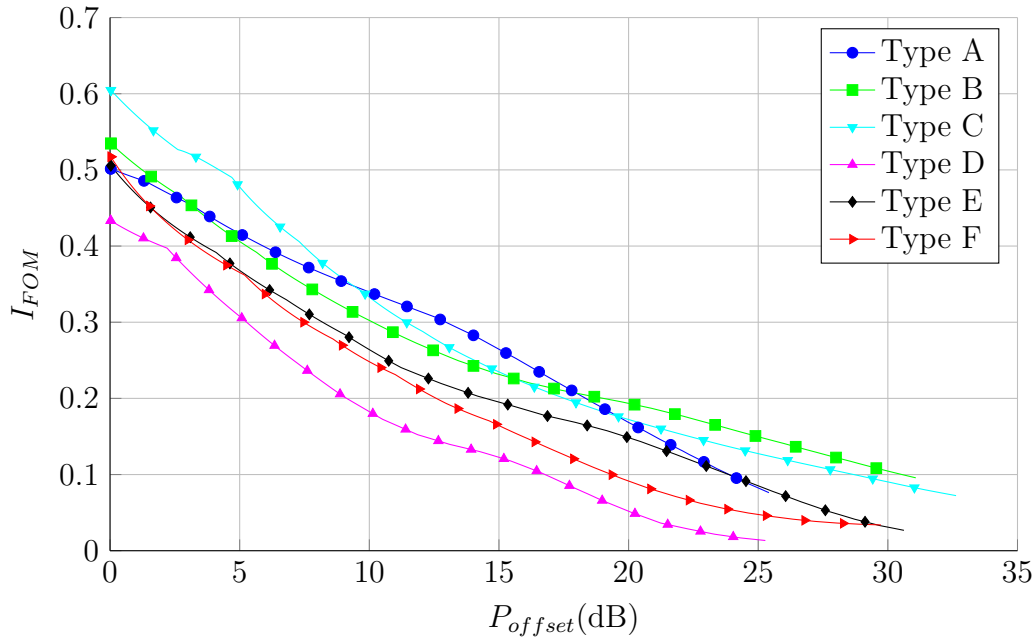


Figure 3.19: Power sweep of $|\Delta\Gamma|$ as function average.

A more conservative value of the maximum value is now seen. Type D also has a more significant lower $|\Delta\Gamma|$ -value over the power sweep.

Finally, I_{FOM} is calculated without and with weighting of $|\Delta\Gamma|$, respectively, shown in Figures 3.20 and 3.21.

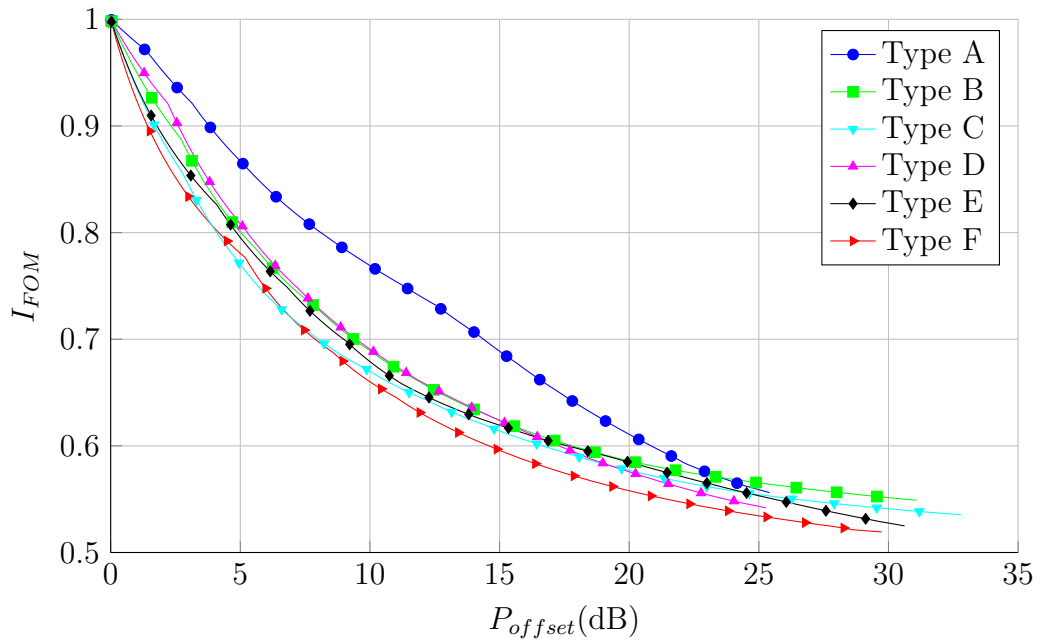


Figure 3.20: FOM sweep without $\Delta\Gamma$.

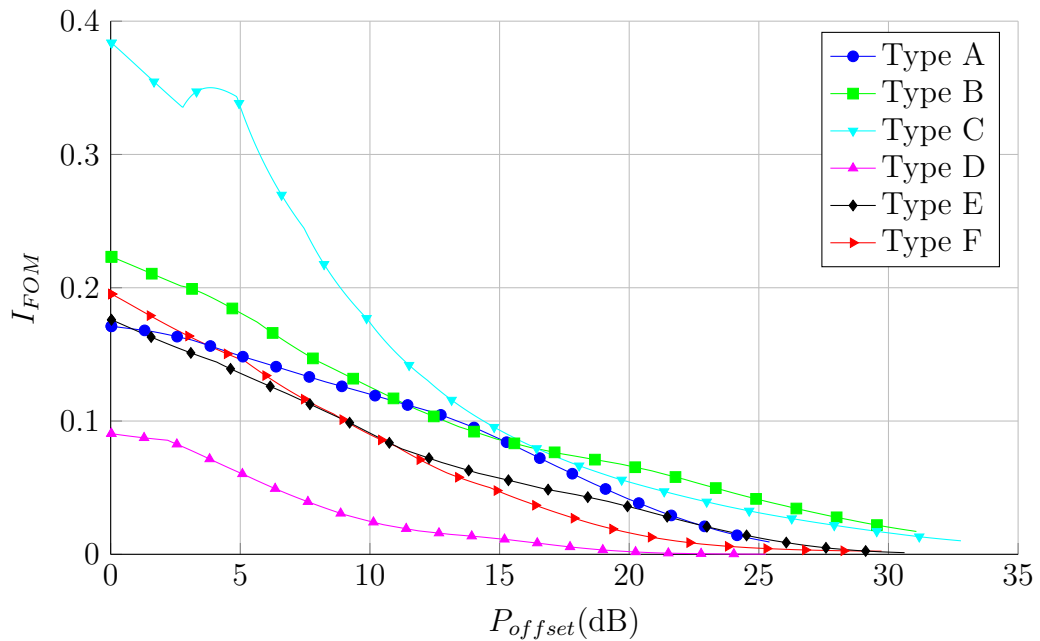


Figure 3.21: FOM sweep with $\Delta\Gamma$.

The results without $|\Delta\Gamma|$ in Figure 3.20 are similar to the fixed source impedance case in Figure 3.18, but it is seen how the mismatch condition for Type D is moved to better performance.

The results in Figure 3.21, including both $|\Delta\Gamma|$ and k_M , are interesting. It can be observed that $|\Delta\Gamma|$ and k_M interact to give bigger differences in performance between the different transponder types, as compared to when they are treated separately. Type C exceeds the remaining types in performance, in the lower half of power offset. Type A, B and C are from the same vendor, of which Type C is the latest released product. For Type D a big difference between excluding and including $\Delta\Gamma$ is seen.

Another observation is the agreement between the FOM calculations and behavior in RFID profiling, as described in Section 1.3. Figure 3.22 shows an example of RFID profiling with big offset between read and write threshold. This means that the drive power has to be increased substantially to enable programming of the transponder as compared to only reading information from it.

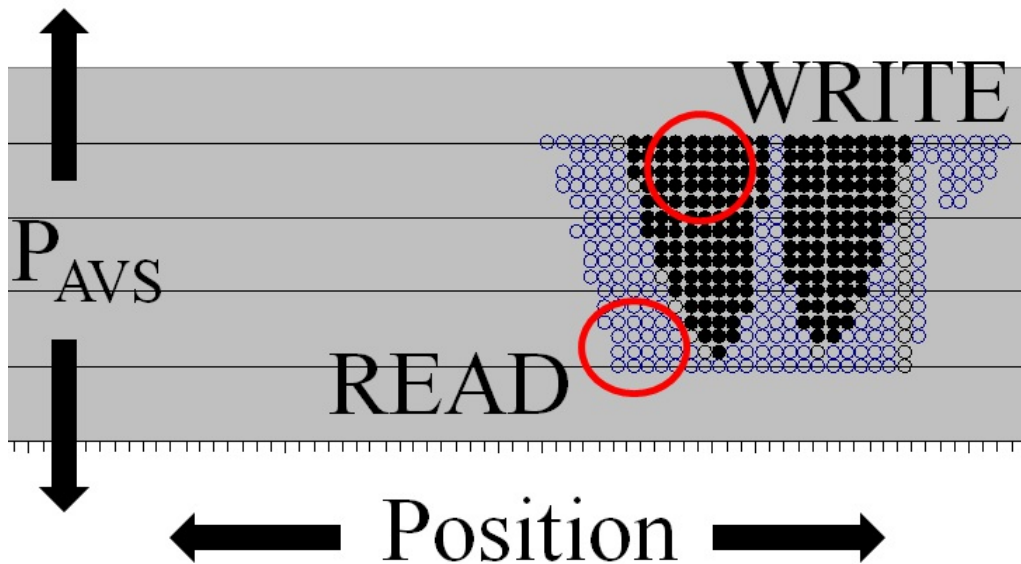


Figure 3.22: An example of RFID profiling with big read/write offset. Empty and full circles indicate read only full read write compatibility, respectively.

One probable explanation for this behavior is that non-linearity has an impact. In particular, big a read/write offset has been seen for Type E and F in RFID profiling. In Figure 3.23 a zoomed in region of Figure 3.21 is shown. It is seen at approximately 1 and 4 dB power offset, respectively, how Type E and F transition from higher to lower values of performance as compared to Type A, although this is not as evident for Type E. Type A is mentioned as reference here since during RFID profiling in particular Type A, E and F were compared.

Type D, which is from the same vendor as for Type C, but an older version, has also shown deviating performance in RFID profiling. Higher drive levels are needed for any type of response, but at this threshold immediate read and write compatibility is achieved. This is also confirmed in Figure 3.20, showing mismatch

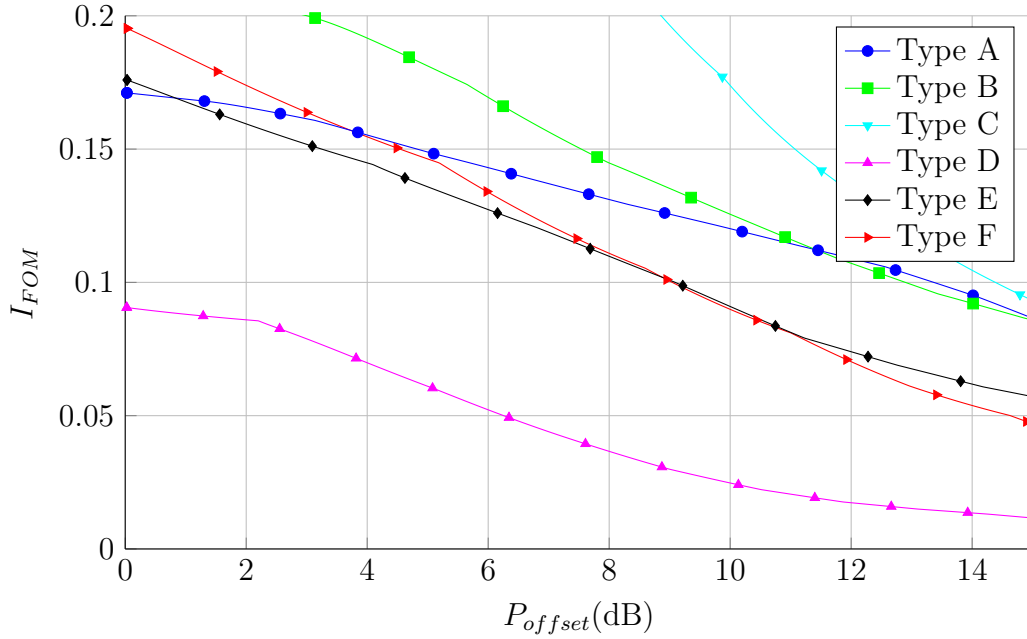


Figure 3.23: FOM sweep with $\Delta\Gamma$ zoomed over low power offset region.

performance only, whereas a degraded performance is shown, when all FOM quantities are included, in Figures 3.21 and 3.23.

3.11 Conclusions FOM characterization

The developed FOM will most importantly give electrical information on performance related to the required adjustment in available power, needed for an arbitrary source, to go from an initial read response to full write compatibility in the transponder. The results show deviating performance between different transponder types, commercially available on the market. A high FOM yields higher flexibility to a change of source impedance, i.e., for a high FOM the mismatch condition does not change drastically during the offset adjustment, independent of the source environment. In other words a reliable reading and writing to the transponder chip can be achieved. It can also be done at low drive power levels. This is another requirement to achieve sufficient electromagnetic isolation in a dense tag environment, such as commonly found in a printer cavity.

Chapter 4

The linear channel between transponder and interrogator

The previous chapters have treated the measurement and characterization of RFID transponders. Much focus has been put on understanding their non-linear behavior, and their part in phenomena occurring in the RFID profiling process. A turn will now be made towards the more field theoretic topic of reactive near field (RNF) coupler technology, for efficient programming of RFID inlays. This will be a starting point of what will be future work after this thesis.

4.1 Two aspects on programming RFID inlays

A coupler can be seen as being part of a linear channel, describing the intermediate environment between the transponder RF frontend and the antenna port of the interrogator, with one of main challenges being the highly efficient electromagnetically isolated communication with a single inlay in a dense environment of several. Two main aspects exist on the programming of RFID inlays in the RNF. One is the spatial selection, mainly in two dimensions, by means of electromagnetic phase manipulation. This problem is also evident from the discussion in Chapter 1. The other aspect is the coupling efficiency of a single coupling element, in an array arrangement of multiple elements.

The channel may generally be represented by a two-port S -parameter network (LNW), as illustrated in Figure 4.1. The LNW may be thought of as incorporating also spatial selectivity, in the sense that if the inlay is located anywhere within an active area of the coupling arrangement, a regulatory functionality assures excitation of the transponder. Depending on the level of efficiency the LNW also incorporates resistive losses, being equivalent to any internal losses and outward radiation.

Given this representation, a tool set traditionally used in amplifier theory is provided for a general analysis, without any consideration needed to any specific coupler architecture [25]. Later, in the coupler design process specifics are treated, but still suitable performance parameters are found in the tool set.

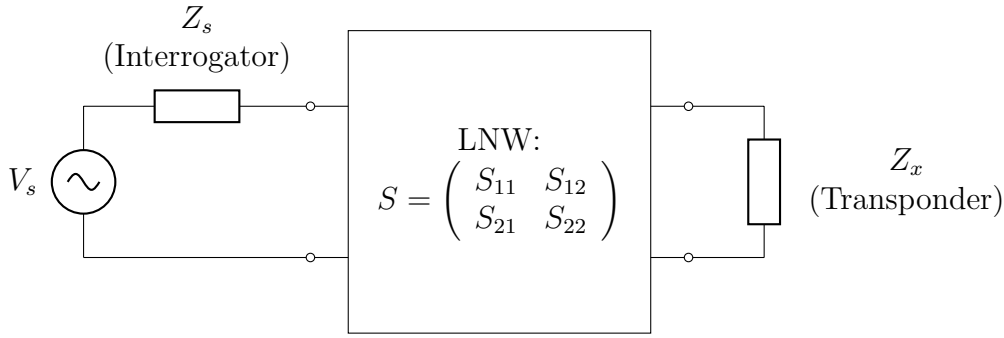


Figure 4.1: The linear channel between transponder and interrogator.

The power transfer from the interrogator to the transponder may generally be described by the transducer gain, given as

$$G_t = \frac{P_L}{P_{AVS}} = \frac{(1 - |\Gamma_s|^2) |S_{21}|^2 (1 - |\Gamma_x|^2)}{|(1 - S_{11}\Gamma_s)(1 - S_{22}\Gamma_x) - S_{12}S_{21}\Gamma_s\Gamma_x|^2} \quad (4.1)$$

which takes into account mismatch between the interrogator and the LNW, as well as between the transponder and the LNW. Matching of the input at the interrogator side implies $\Gamma_{in} = \Gamma_s^*$, where

$$\Gamma_{in} = S_{11} + \frac{S_{12}S_{21}\Gamma_x}{1 - S_{22}\Gamma_x} \quad (4.2)$$

which is the definition of power gain. The power gain, or operating power gain, is obtained as

$$G_p = \frac{|S_{21}|^2 (1 - |\Gamma_x|^2)}{|1 - S_{22}\Gamma_x|^2 - |S_{11}(1 - S_{22}\Gamma_x) + S_{12}S_{21}\Gamma_x|^2} \quad (4.3)$$

when the conjugate of (4.2) is substituted into (4.1).

Power gain, calculated in a coupling circuit would tell how high coupling can possibly be achieved since the input is perfectly matched, and any power not delivered to the load is dissipated in the channel. Hence, power gain is a good measure of efficiency. It turns out that in a realistic case, high power gain is often accompanied with bandwidth limitations, a high Q -value. Some form of resistance is needed to achieve an acceptable operational bandwidth.

4.2 Q -value reduction

In the case of transponder chips, a wired two port measurement of the LNW is difficult, or even impossible to carry out. The obvious reason is the connection interface between the inlay antenna and the transponder chip, which is not a standard interface. Analysis of potential coupling efficiency and internal losses are done with

finite element (FEM) software, on which any realizations are based. At a particular frequency, if a value of power gain is available, internal losses may be analyzed by phase compensating the input of the LNW and measuring the input resistance, R_{in} . Let the internal losses be represented by a resistance R_i . Since power gain restricts the source resistance to be $R_s = R_{in}$, the power delivered to the load is

$$G_p P_{AVS} = \frac{G_p |V_s|^2}{8R_{in}} = P_{AVS} - \frac{|V_s|^2}{8R_i} = P_{AVS} \left(1 - \frac{R_{in}}{R_i}\right) \iff R_i = \frac{R_{in}}{1 - G_p}. \quad (4.4)$$

For a high Q circuit R_i has a high value (parallel topology). Assume that a back down of delivered power is allowed to a value denoted $P_{x,min}$, where $G_p \geq P_{x,min}/P_{AVS}$. A modification of 4.4 for increased bandwidth, by means of an additional resistor at the input, would be

$$R_{i,min} = \frac{R_{in}}{1 - \frac{P_{x,min}}{P_{AVS}}}. \quad (4.5)$$

4.3 Sensitivity enhancement

With reference to Figure 4.1, consider the reflection coefficients Γ_x and Γ_{in} at the transponder (load) plane and at the LNW input plane, respectively. Any deviation in the passive transponder impedance Z_x from a nominal value, say Z_{x0} , will be constrained to be located inside the Smith chart. In the general complex plane, in order to avoid negative resistance, a deviation ϵ will be defined according to a disk with circumference having center and radius given as

$$C_0 = \frac{\text{Re}\{Z_{x0}\} + \epsilon}{2} + j\text{Im}\{Z_{x0}\} \quad r_0 = \frac{\text{Re}\{Z_{x0}\} + \epsilon}{2}. \quad (4.6)$$

As $\epsilon \rightarrow \infty$, $\{C_0, r_0\}$ will cover all possible values of Z_x . Using the recipe from Appendix B, $\{C_0, r_0\}$ with the bilinear mapping taken as (3.16) will map to another circle in the Γ_x -plane, with center and radius given as

$$C_x = \frac{(C_0 + Z_0)^*(C_0 - Z_0) - r_0^2}{|C_0 + Z_0|^2 - r_0^2} \quad r_x = \frac{2r_0 Z_0}{\left||C_0 + Z_0|^2 - r_0^2\right|}. \quad (4.7)$$

The final mapping from the Γ_x -plane to the Γ_{in} -plane, now using (4.2) as the bilinear mapping and again using the recipe, is given as

$$C_{in} = \frac{r_x^2 S_{22}^* \Delta + (1 - S_{22} C_x)^*(S_{11} - \Delta C_x)}{|1 - S_{22} C_x|^2 - r_x^2 |S_{22}|^2} \quad r_{in} = \frac{r_x |S_{12} S_{21}|}{\left||1 - S_{22} C_x|^2 - r_x^2 |S_{22}|^2\right|} \quad (4.8)$$

with $\Delta = S_{11} S_{22} - S_{12} S_{21}$. At this point only reciprocity holds. As an approximation for a highly efficient coupler circuit, assume now that the internal losses may be neglected ($R_{i,min}$ very large), leading to

$$S_{12} = S_{21} \quad |S_{11}| \approx |S_{22}| \quad |S_{12}|^2 \approx 1 - |S_{11}|^2. \quad (4.9)$$

Further consider the input of the LNW as matched with $S_{22} = \Gamma_{x0}^*$. The radius of (4.8) can then be written

$$r_{in} = \frac{r_x (1 - |S_{22}|^2)}{\left| |1 - S_{22}C_x|^2 - r_x^2 |S_{22}|^2 \right|}. \quad (4.10)$$

Not much can be said about how r_{in} will behave relative to r_x , which is of interest here. An illustration of the situation is shown in Figure 4.2

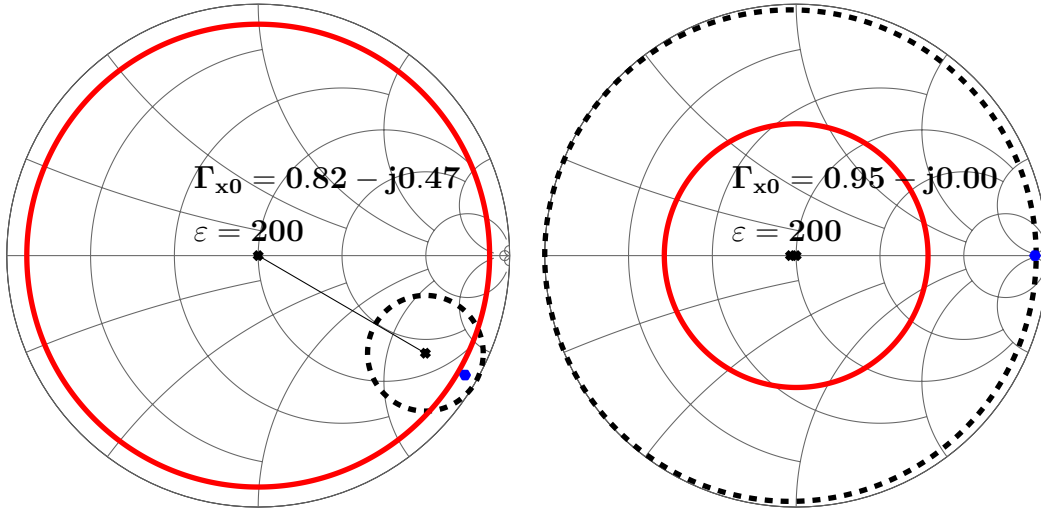


Figure 4.2: Two different cases of Γ_{x0} location.

Clearly, no particular trend of the relation between r_{in} and r_x is seen, since there is a dependency on location of the load impedance Γ_{x0} . The right plot of Figure 4.2 shows the case of Z_{x0} being real and highly resistive. From (4.6) and (4.7) it is seen that $C_x \rightarrow 0$ and $r_x \rightarrow 1$, respectively. To say any more, some restriction is needed on Γ_x (S_{22}^*). A realistic assumption is the low real part and highly capacitive reactive part of the transponder, so that Γ_{x0} is always located, roughly, as shown in the left plot of Figure 4.2. In this case from (4.10), using the symmetry for a growing ϵ , $\arg(C_x) \approx \arg(S_{22}^*)$ so that $C_x = \gamma S_{22}^*$ for some real $\gamma \in [0, 1)$. Further, rearrangement of (4.7), using (4.6), shows that $r_x = 1 - |C_x|$ (a rather obvious fact when observed graphically). Now (4.10) is rewritten as

$$\begin{aligned} r_{in} &= \frac{r_x (1 - |S_{22}|^2)}{\left| (1 - \gamma |S_{22}|^2)^2 - r_x^2 |S_{22}|^2 \right|} = \frac{r_x (1 - |S_{22}|^2)}{\left| (1 - \gamma |S_{22}|^2)^2 - (1 - \gamma |S_{22}|)^2 |S_{22}|^2 \right|} \\ &= \frac{r_x (1 - |S_{22}|^2)}{(1 - \gamma |S_{22}|^2)^2 (1 - |S_{22}|^2)} > r_x \end{aligned} \quad (4.11)$$

In summary it has been proved that, provided $\arg(C_x) \approx \arg(S_{22}^*)$, always $r_{in} > r_x$. A graphical illustration of this fact is shown in Figure 4.3.

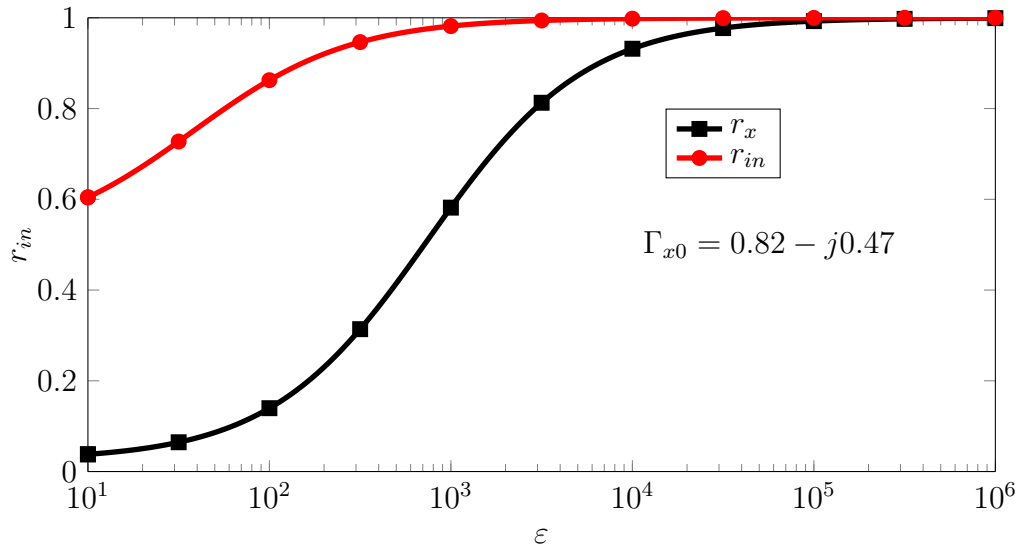


Figure 4.3: The difference between r_x and r_{in} when $\arg(C_x) \approx \arg(S_{22}^*)$.

As the transponder impedance shifts, the value of ε yielding the circle $\{C_{in}, r_{in}\}$ on which the shifted impedance is located, will always imply an increase in r_{in} , or in other words an increase in sensitivity at the input of the two-port transformation. This will come handy when considering the $|\Delta\Gamma|$ -value for an efficient coupler, having low internal losses.

Chapter 5

Spatial selection by phase manipulation

In an array configuration of reactive near field (RNF) coupling elements, where several elements are active at the same time, some form of phase manipulation is needed for the coupling to achieve a consistent current flow on the energized inlay, and not cause any destructive interference. This means that not only the coupling element itself needs to be efficient, but also all elements being part of the active set need to interact in a constructive way. One exemplary investigation of this concept is presented in Paper C, in the case of the segmented transmission line (TRL).

5.1 Lumped component phase compensation

A summary of the important theoretic results from Paper C follows. The theoretic analysis starts with the basic traveling wave equations for a TRL, with characteristic impedance Z_c , according to

$$\begin{cases} V(\theta) = V^+ e^{-j\theta} + V^- e^{j\theta} \\ I(\theta) = \frac{1}{Z_c} (V^+ e^{-j\theta} - V^- e^{j\theta}). \end{cases} \quad (5.1)$$

Manipulation leads to the voltage/current transfer matrices, which may either relate input to output quantities, or vice versa, as

$$\begin{pmatrix} V_2 \\ I_2 \end{pmatrix} = A_1 \begin{pmatrix} V_1 \\ I_1 \end{pmatrix} \quad \begin{pmatrix} V_1 \\ I_1 \end{pmatrix} = B'_1 \begin{pmatrix} V_2 \\ I_2 \end{pmatrix} \quad B'_1 = A_1^{-1}. \quad (5.2)$$

The result is

$$A_1 = \begin{pmatrix} \cos \theta & -jZ_c \sin \theta \\ -j\frac{\sin \theta}{Z_c} & \cos \theta \end{pmatrix} \quad B'_1 = \begin{pmatrix} \cos \theta & jZ_c \sin \theta \\ j\frac{\sin \theta}{Z_c} & \cos \theta \end{pmatrix}. \quad (5.3)$$

Both of these representations are used.

A phase compensation network, valid for a short electrical length θ_0 (segment), where $\cos \theta_0 \approx 1$, is the simple series/shunt C/L circuit, which is also known as a

lossless left hand transmission line element with high pass filter characteristics [36]. Let the voltage/current transfer matrix of the phase compensation network be denoted B'_2 . The condition for phase compensation at angular frequency $\omega_0 = \sqrt{\varepsilon_{eff}}cl\theta$ is $B' = B'_1 B'_2 = I$, with I the identity matrix. ε_{eff} is the effective dielectric constant of the TRL. c and l are the speed of light and physical TRL length, respectively. Hence, θ principally corresponds to frequency, with given physical parameters, so $\omega_0/\omega = \theta_0/\theta$. The network with fixed values of C and L , under the phase compensation condition, is given in Figure 5.1.

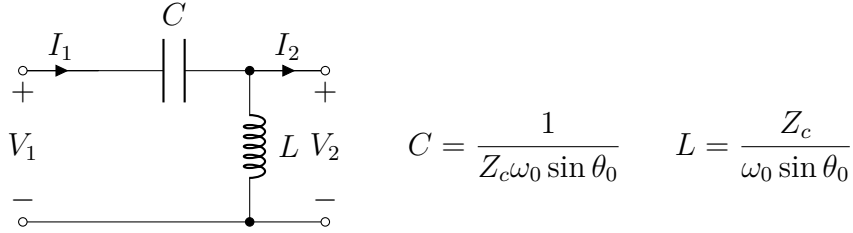


Figure 5.1: Phase compensation network.

This leads to a matrix B of the phase compensated segment, given as

$$\begin{pmatrix} V_1 \\ Z_c I_1 \end{pmatrix} = B \begin{pmatrix} V_2 \\ Z_c I_2 \end{pmatrix}$$

$$B = \begin{pmatrix} \left(1 - \frac{\theta_0^2}{\theta^2} \sin^2 \theta_0\right) \cos \theta + \frac{\theta_0}{\theta} \sin \theta \sin \theta & j \left(\sin \theta - \frac{\theta_0}{\theta} \sin \theta \cos \theta\right) \\ j \left(\sin \theta - \frac{\theta_0^2}{\theta^2} \sin^2 \theta_0 \sin \theta - \frac{\theta_0}{\theta} \sin \theta \cos \theta\right) & \frac{\theta_0}{\theta} \sin \theta \sin \theta + \cos^2 \theta \end{pmatrix}. \quad (5.4)$$

Note that the conversion from B' to B results from the elimination of Z_c from B' . Hence, B only depends on θ . The relation (5.4) is for one compensated segment. The relation for a complete segmented line, consisting of n segments and terminated in a load Z_l , is simply subject to multiplication n times. The input to output voltage and current relationships are written

$$\begin{pmatrix} V_{in} \\ Z_c I_{in} \end{pmatrix} = B^n(\theta) \begin{pmatrix} Z_l I_l \\ Z_c I_l \end{pmatrix} = C(\theta) \begin{pmatrix} Z_l I_l \\ Z_c I_l \end{pmatrix} \quad C = \begin{pmatrix} c_{11} & c_{12} \\ c_{21} & c_{22} \end{pmatrix}. \quad (5.5)$$

The quotients $\alpha = Z_l/Z_c$ and $\beta = Z_c/Z_0$ are now introduced for a qualitative analysis. They are called load impedance level and impedance level, respectively. From these definitions and (5.5) the input impedance and output/accepted input current ratio are directly derived as

$$Z_{in} = \frac{\alpha c_{11}(\theta) + c_{12}(\theta)}{\alpha c_{21}(\theta) + c_{22}(\theta)} \beta Z_0 = \delta(\alpha, \theta) \beta Z_0 \quad r_{I,a} = \frac{I_l}{I_{in}} = \frac{1}{\alpha c_{21}(\theta) + c_{22}(\theta)}. \quad (5.6)$$

The quantity δ defines the dependency on α and θ . For fixed $\theta = \theta_0$, $\delta(\theta_0, \alpha) = \delta_0$, only depending on α . It is noted that C is close to real when $\theta \rightarrow \theta_0$. Hence, a

valid simple match, serving as reference, is the quarter wave transformer ($\lambda/4$ -TRL). The characteristic impedance of the transformer is $Z_{C,\lambda/4} = \sqrt{Z_0 Z_{in}(\alpha, \theta_0)} = Z_0 \sqrt{\delta_0 \beta}$ and the electrical length is $\theta_{\lambda/4}$. If the transformer has the same effective dielectric constant as the segmented TRL, $\theta_{\lambda/4}$ will have the same frequency dependence as θ but at the center frequency $\theta_{\lambda/4} = \frac{\pi}{2}$. This is no loss of generality since for different physical line widths such as for a microstrip the physical length can be adjusted accordingly in the realization. Note that fringing effects are not taken into account. The circuit schematic for the entire circuit is shown in Figure 5.2.

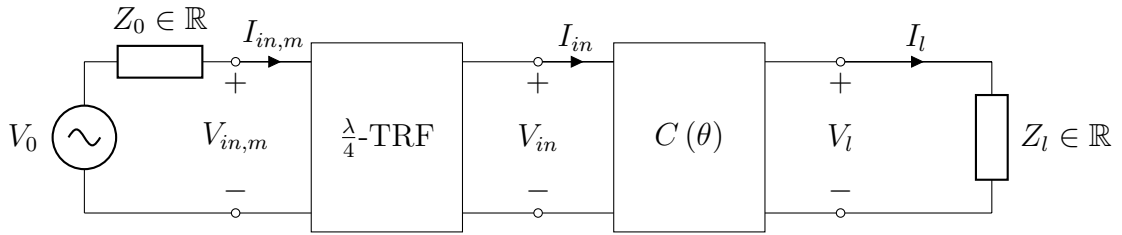


Figure 5.2: Matched phase compensated segmented line.

Manipulation of the expression for input impedance Z_{in} in (5.6), with the given notations, yields the return loss given as

$$RL[\text{dB}] = -20 \log \left| \frac{\sqrt{\delta_0 \beta}(\delta\beta - 1) + j\beta(\delta_0 - \delta) \tan \theta_{\lambda/4}}{\sqrt{\delta_0 \beta}(\delta\beta + 1) + j\beta(\delta_0 + \delta) \tan \theta_{\lambda/4}} \right| \quad (5.7)$$

Denote $BW = \Delta\omega/\omega_0 = \Delta\theta/\theta_0$ the relative bandwidth of acceptable return loss. This is the frequency span where the required return loss is satisfied according to

$$BW = \Delta\omega/\omega_0 = \Delta\theta/\theta_0 \quad (5.8)$$

with

$$\theta \in \theta_0 \left[1 - \frac{BW}{2}, 1 + \frac{BW}{2} \right], \quad \theta_{\lambda/4} \in \frac{\pi}{2} \left[1 - \frac{BW}{2}, 1 + \frac{BW}{2} \right]. \quad (5.9)$$

Again manipulation of the expressions A_1 in (5.3), for $\lambda/4$ -TRL, and Z_{in} in (5.6) yields an expression for the output/matched input current ratio, given as

$$r_{I,m} = \frac{I_l}{I_{in,m}} = \frac{(\sqrt{\delta_0 \beta} + j\delta\beta \tan \theta_{\lambda/4}) \cos \theta_{\lambda/4} + (\sqrt{\delta_0 \beta} \tan \theta_{\lambda/4} - j\delta\beta) \sin \theta_{\lambda/4}}{(\alpha c_{21} + c_{22})(\sqrt{\delta_0 \beta} + j\delta\beta \tan \theta_{\lambda/4})}. \quad (5.10)$$

BW , $r_{I,a}$ and $r_{I,m}$ are the quantities of interest in the predicted results.

5.2 Predicted frequency dependency

In the results the case $\beta = 0.28$ ($Z_c = 14 \Omega$) and $\theta_0 = 10^\circ$ is considered. The 15 dB relative bandwidth ($BW_{15\text{dBRL}}$) and $|r_{I,m}|$ as functions of α are plotted in Figure 5.3 for different values of n .

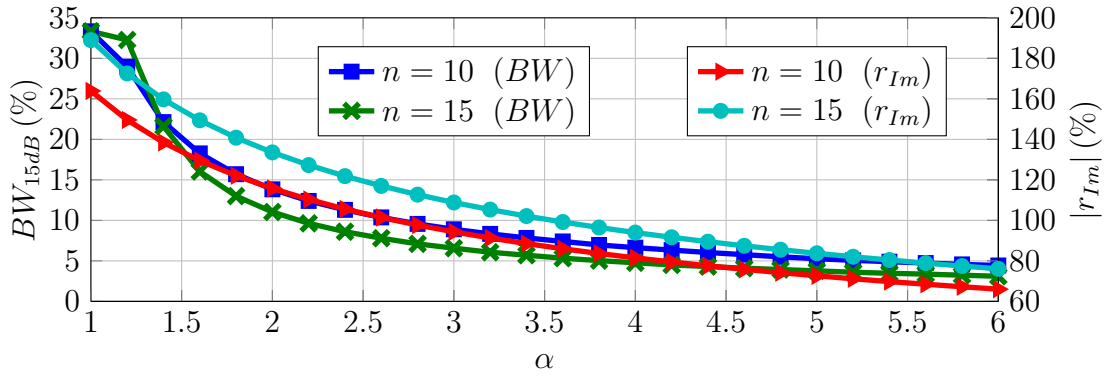


Figure 5.3: 15 dB return loss bandwidth and the output/matched input current magnitude ratio as functions of α .

It is seen that the lowest values of α also give the highest bandwidths. For a low value of β there is a transformation to higher currents on the line, which are suitable for high magnetic coupling. Side effects like fringing capacitances give practical limits to the matching.

In Figure 5.4 magnitude and phase of $r_{I,m}$ and $r_{I,a}$, respectively, are plotted as functions of θ . In this case $\alpha = 1$ ($Z_l = Z_c$).

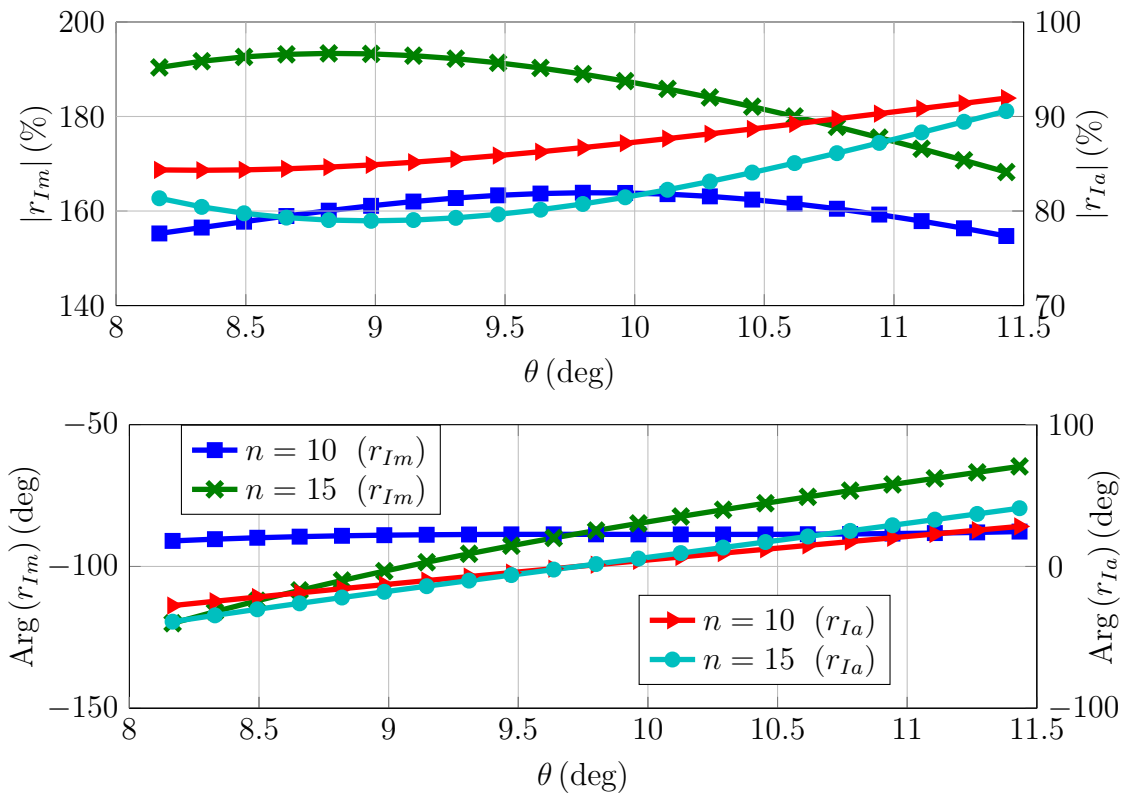


Figure 5.4: Current ratios as functions of θ for $\alpha = 1$.

The main observation is that magnitude and phase do not change much along the line. However, the matching and resulting transformation of current magnitude creates a shift between the matched input and the line. There is also a limitation in frequency over which the phase compensation still holds.

5.3 Simulated results and fabrication

A demonstrator with $n = 15$ was modeled in a FEM simulation and then fabricated. The PCB is a 5 by 95 mm three layer RogersTM 4350 0.254 mm thick substrate. In particular the FEM simulated phase shift and return loss for the phase compensated segmented line, were compared with the unsegmented line, as shown in Figure 5.5. Distributed spiral inductors were chosen, as seen at the top of Figure 5.5.

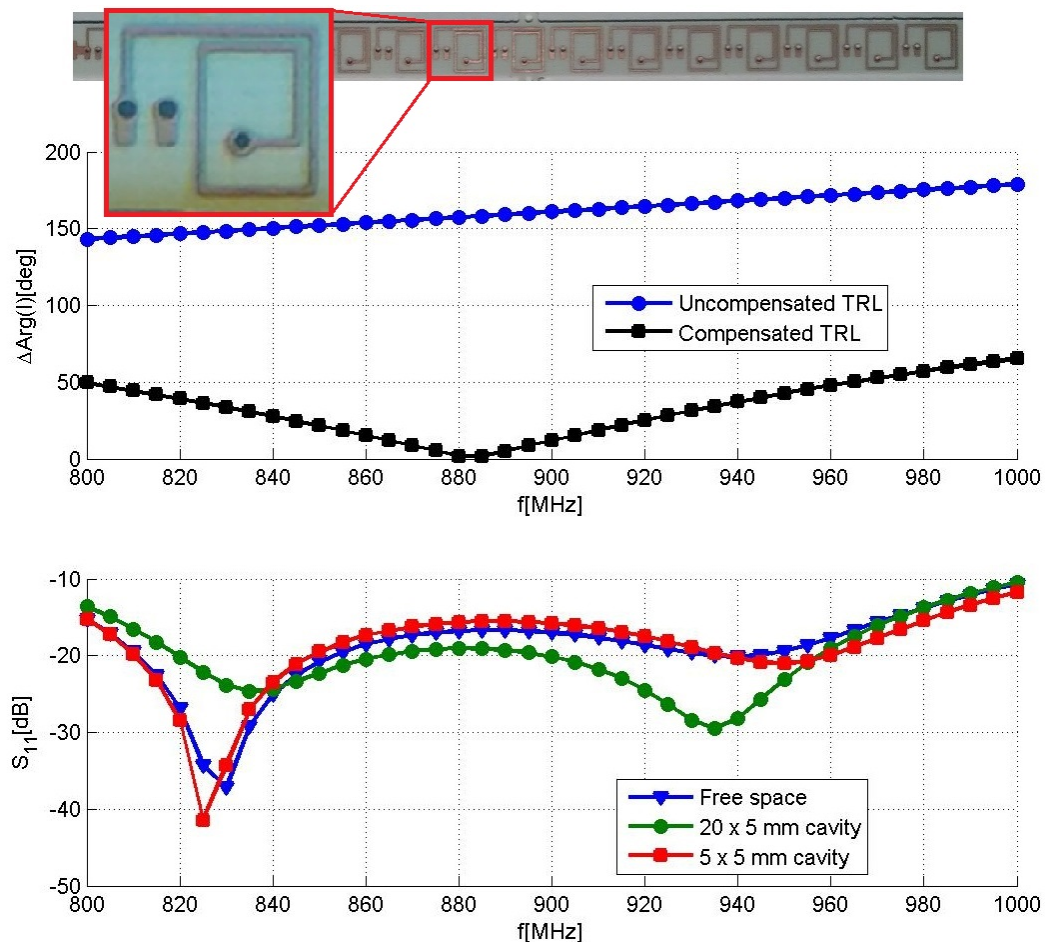


Figure 5.5: Top: Spiral inductor realization. Middle: Current phase shift from input to output for 20 x 5 mm cavity as compared to a straight uncompensated TRL of the same physical length. Bottom: Return loss for different cavities.

A big difference is seen in phase shift, whereas the return loss is approximately equal, having a value above 15 dB over the 860-960 MHz operating band.

Further, from the FEM simulated results, which include fringing and other electromagnetic effects, an accepted current magnitude ratio of $r_{I,a} = 62\%$ is achieved, compared with the theoretical prediction of 81% , found in Figure 5.4. The unsegmented value is 28% . Further details on parameter values are given in Paper C.

5.4 RFID profiling results

Six different inlay design were chosen for RFID profiling, see Paper C. The interpretation of the RF window is explained in Section 1.3. One of the results is shown in Figure 5.6.

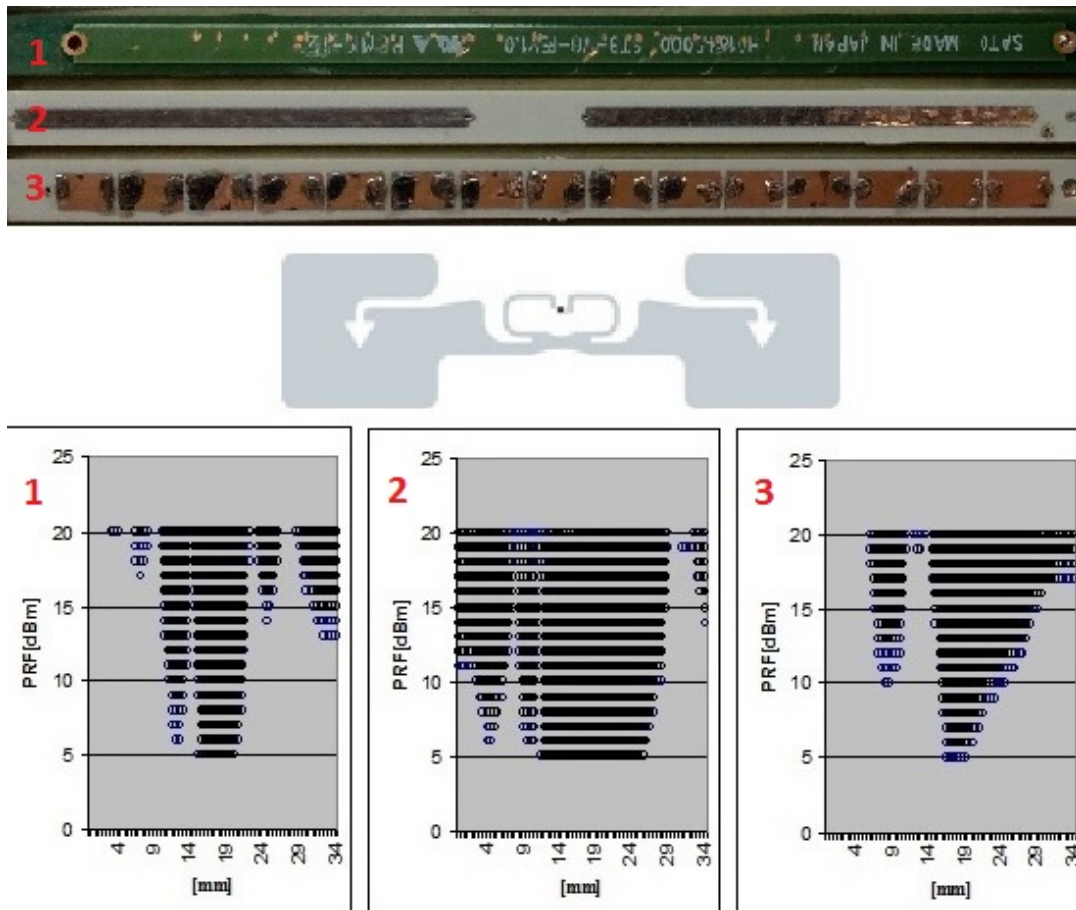


Figure 5.6: Example of RFW profile for one of the tested inlay types.

As comparison the simple straight unsegmented TRL coupler (1) and a dual patch TRL coupler, with balanced signal configuration (2), were also tested with this inlay [6]. Note that the TRL segment side is shown of the segmented coupler (3), as compared with Figure 5.5.

The profiling results for the remaining five inlay types are similar. In summary it is concluded that the segmented TRL, with the TRL segments as coupling elements

is not optimized for coupling in the spatial sense. Yet still, another purpose in Paper C was to demonstrate the concept of phase compensation. Good bandwidth is achieved for an element count up to 15. The inductors were chosen as distributed elements. The reason, at the time of writing Paper C, was to avoid the use of too many lumped components and difficulty in obtaining small form factor chips commercially. However, the use of distributed inductors is an interesting point, in the distributive sense. As will be presented in the next chapter, TRL based inductive loops as coupling elements will be used. Hence, the phase compensating concept, as demonstrated in Paper C, may become useful in the future for array configurations. Array solutions are beyond the scope of this thesis.

Chapter 6

The differential transmission line loop as efficient coupling element

The differential transmission line loop (DTLL) is an extension of the transmission line (TRL) based reactive near field (RNF) coupling concept, with focus on higher efficiency. The high coupling factors are achieved by taking into account the inductive current loop of the inlay. Promising results for a number of different inlay geometries are seen, when also using several different DTLL geometries.

6.1 The inlay inductive loop as coupling target

Figure 6.1 shows a FEM model of an inlay located on a substrate (upper layer) with a ground plane beneath (lower layer), and another identical inlay located 1 mm above the former one. The inlay located above the substrate is called coupling geometry (CG) and the inlay above, which is the one under motion is called inlay geometry (IG).

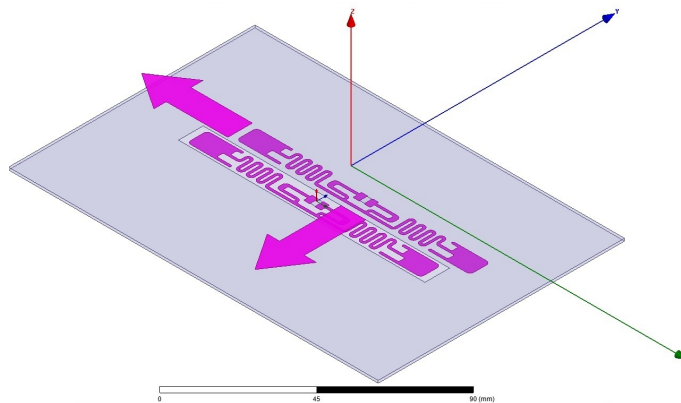


Figure 6.1: The relative motion of two identical inlay geometries.

IG is a commercially available inlay, optimized for performance in the far field. Yet still, despite the close location to the ground plane, it was realized that a strong

electromagnetic interaction exists between CG and IG, when the inductive loops of the CG and IG are aligned. This suggests a spatially selective RNF interaction. Both the ports on the CG and IG are differentially fed. Furthermore, as shown in the FEM simulations, far field radiation is strongly suppressed, due to the ground plane.

From the discussion so far two properties are identified. One is the differential feeding. The other is the presence of a ground plane. In Paper D these properties are exploited by means of the differential transmission line loop (DTLL).

6.2 Properties of the DTLL

The DTLL is a differential fed transmission line, where the input and output of the line act as a differential port. Physically the terminals are located close together so that the transmission line forms a loop.

The governing voltage/current traveling wave relations for a differentially fed finite TRL segment, with length l and propagation factor γ , are given by [37]

$$\begin{cases} V^+ + V^- = V \\ V^+ e^{-\gamma l} + V^- e^{\gamma l} = -V. \end{cases} \quad (6.1)$$

In the low loss approximation $V^+/I^+ = V^-/I^- = Z_c$, where Z_c is the characteristic impedance, so that the differential input impedance $Z_{DTLL} = 2V/I$, after manipulation of (6.1), can be written as

$$Z_{DTLL} = 2Z_c \tanh\left(\frac{\gamma l}{2}\right). \quad (6.2)$$

This corresponds to the short circuited single ended TRL with double the characteristic impedance and half the length [37].

Due to the TRL nature, the DTLL is a poor radiator. Hence, the real part of Z_{DTLL} is well approximated by the losses of the TRL itself. Thus the DTLL has a high Q -value, which is increased due to the presence of a ground plane. The theory of reducing the Q -value and gaining bandwidth, by adding resistance, is covered in Section 4.2. The result for a phase compensated input is

$$R_{i,min} = \frac{R_{in}}{1 - \frac{P_{e,min}}{P_{AVS}}}. \quad (6.3)$$

In Paper D $R_{i,min} = 500 \Omega$. This is still considered to be a high value. The value of phase compensation (C_{PC}) depends on the DTLL length.

6.3 Design

Four types of super elliptical DTLL loop geometries are considered, as shown in Figure 6.2. They are denoted CG1-CG4.

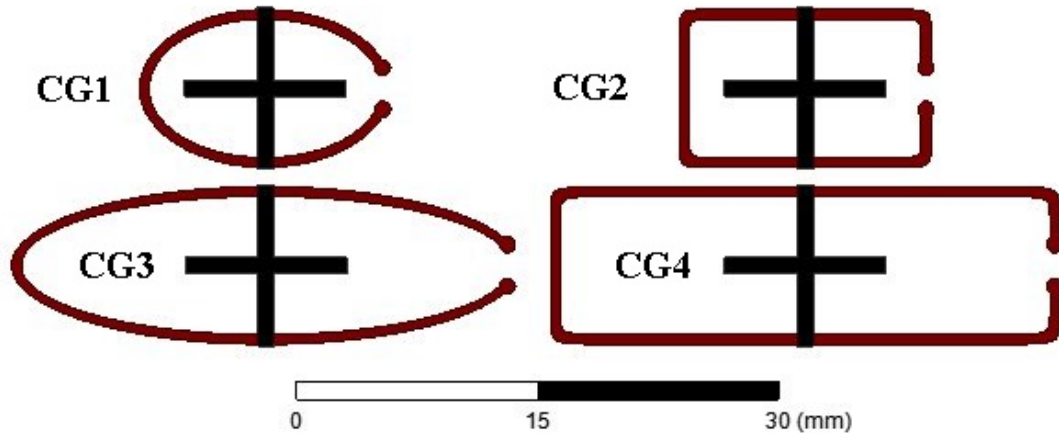


Figure 6.2: Chosen loop geometries.

The DTLL requires differential feeding and the realization is based on a dual lattice balun [38] according to Figure 6.3.

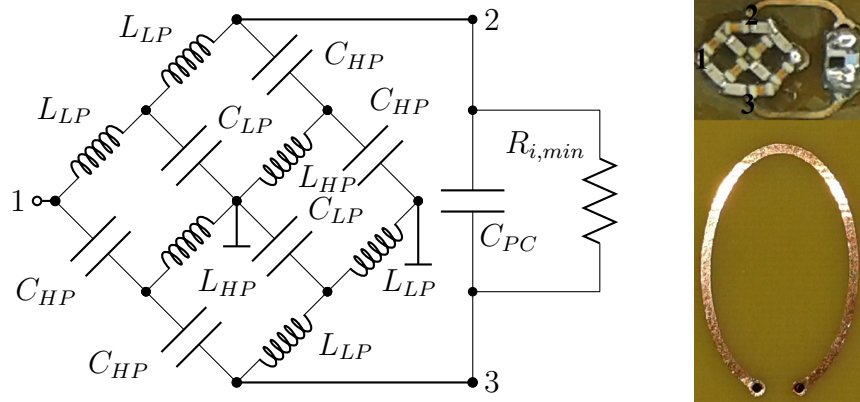


Figure 6.3: Left: Circuit topology of component side, including balun, phase compensation, and Q -value reduction ($R_{i,min}$). Right: Realization of component side (top) and loop side (bottom).

The component values are listed in Table 6.1, for operation at 925 MHz. The resistor $R_{i,min}$ approximates the input resistance of the phase compensated DTLL well, due to the low TRL losses. Hence, the impedance transformation factor is roughly $k = 5$. The balun measures 5 by 4 mm, using 0402 (1 by 0.5 mm) components for compact size. The PCB is in three layer FR4 technology.

In Figure 6.3 CG1 is shown. The four types of super elliptical geometries considered are not the only ones. Other shapes than super elliptical ones are possible. The reason why it is chosen in Paper D, is the many shapes that may be created by only varying a few parameters in the super ellipse equation. From the design it is

Table 6.1: Chosen component values.

L_{LP} (nH)	C_{LP} (pF)	L_{LP} (nH)	C_{HP} (pF)	C_{PC} (pF)	$R_{i,min}$ (Ω)
20	1.0	24	1.8	0.9 (CG1) 0.5 (CG2)	500

seen that many possibilities exist, of varying both the choice of component values and loop geometry of the DTLL.

Six inlay geometries are considered, as shown in Figure 6.4. They are denoted IG1-IG6. To clarify what the inductive loop of an inlay is, consider Figure 6.5, which includes yet another geometry. Clearly, the geometry of the inlay may look very different. The shown geometries are only a few of a vast number that exist and are available commercially on the market. However, a common feature found in all variants is the inductive loop, as indicated in dashed.

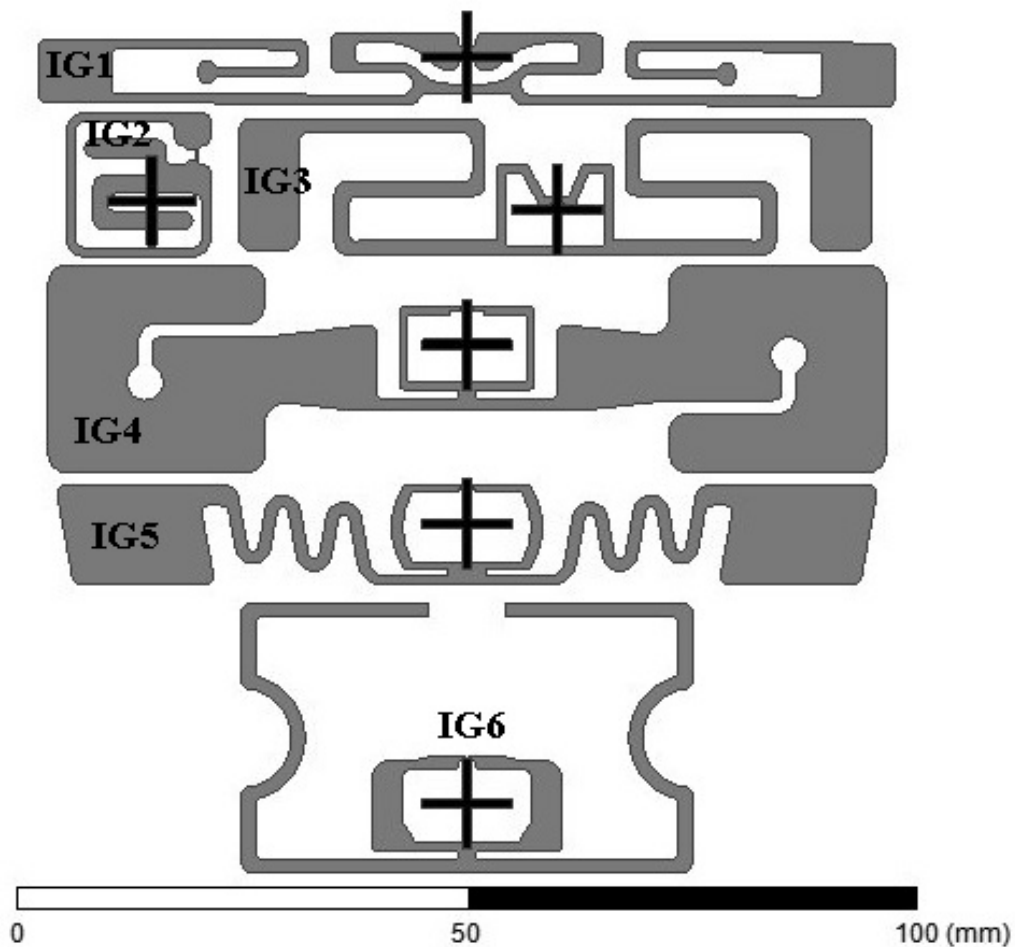


Figure 6.4: Chosen inlay geometries.

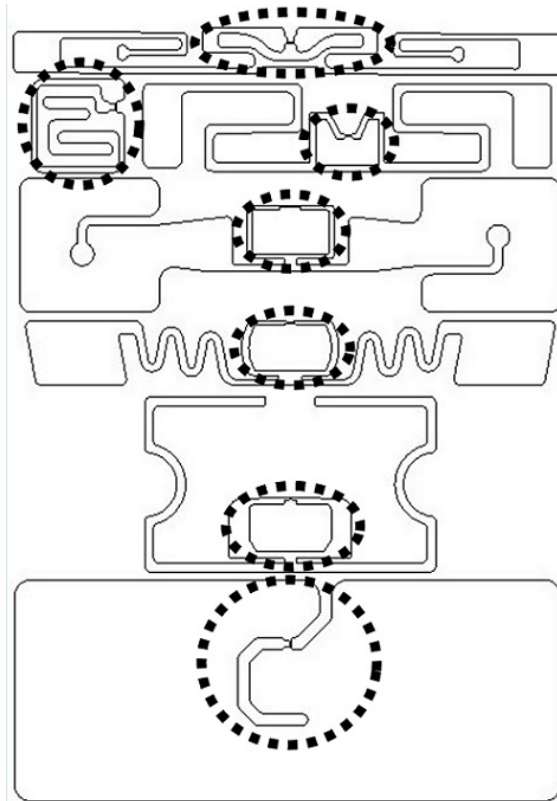


Figure 6.5: Inductive loops of inlays).

6.4 Results

The measurement setup is shown Figure 6.6.

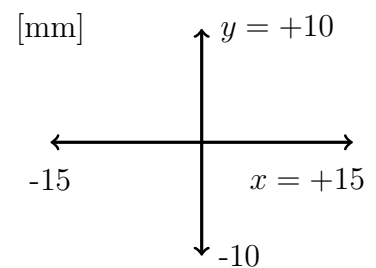
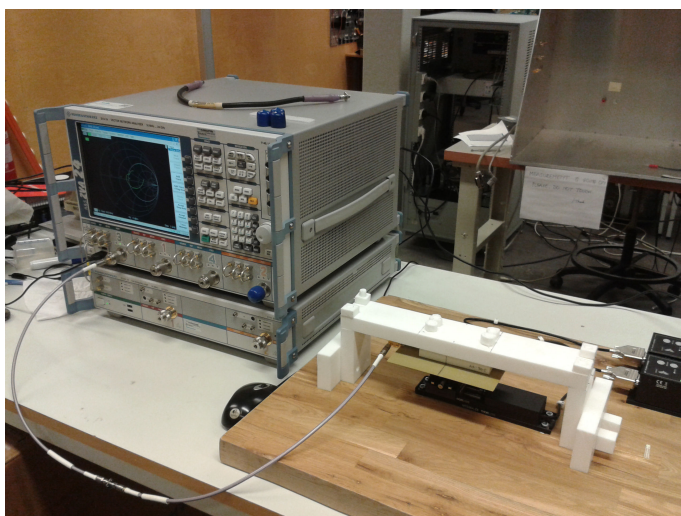


Figure 6.6: Right: Measurement setup. Left: Motion sequence.

Basically the same measurement is used as in the transponder characterization, covered in Section 3.6.1, but in Paper D focus is put in the $|\Delta\Gamma|$ -value (3.22). Further, motion sweeps are included.

One critical aspect on DTLL performance is the practical bandwidth of operation. The measured return loss is shown in Figure 6.7.

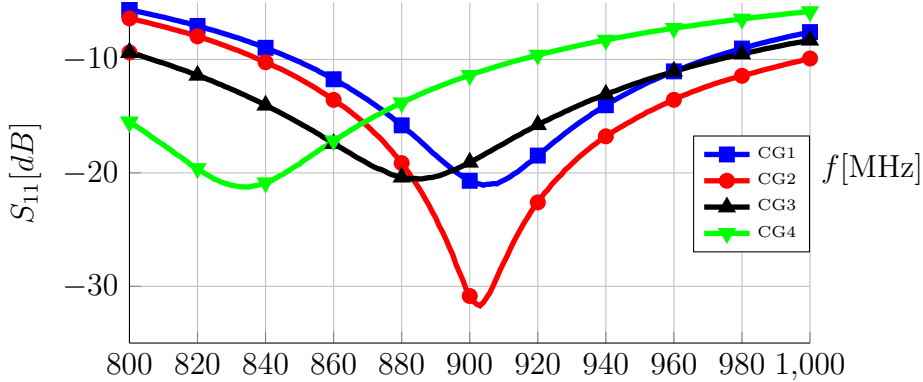


Figure 6.7: Return loss of DTLL for CG1-CG4.

In particular CG1 and CG2 shows satisfactory return loss of 17 dB or higher at 925 MHz with some margin in bandwidth. CG3 and CG4 are shifted in frequency, due to the loop lengths being slightly longer than half a wavelength.

Listed values of coupling, in terms of transducer gain (G_t), $|\Delta\Gamma|$ at 0 dBm and read/write threshold power of a commercial interrogator, at the CG1 peak position, are given in Table 6.2.

Table 6.2: Coupling, $|\Delta\Gamma|$ and input threshold power at peak position.

	Coupling(dB) / $ \Delta\Gamma $ @0 dBm / $P_{AVS0,th}$ (dBm)			
	CG1	CG2	CG3	CG4
IG1	9/0.12/ ± 0	13/0.10/-6	11/0.12/-6	16/0.07/-6
IG2	8/0.35/-5	8/0.46/-6	13/0.17/-2	15/0.09/ ± 0
IG3	11/0.20/-4	12/0.22/-4	19/0.00/+4	21/0.00/+5
IG4	8/0.19/-6	8/0.22/-7	11/0.12/-3	13/0.07/-2
IG5	8/0.26/-7	8/0.35/-7	12/0.20/-3	14/0.09/+1
IG6	9/0.19/-6	8/0.25/-5	11/0.14/-3	13/0.13/-1

From Table 6.2, values of $|\Delta\Gamma| = 0.1$ correspond to $P_{AVS0,th} = 0$ dBm, as seen in the CG1/IG1 and CG4/IG2 cases. However, threshold power levels as high as 5 dBm are considered as very low in RNF encoding of RFID inlays. Clearly, all cases in Table 6.2 indicate strong coupling, when compared with the corresponding threshold powers.

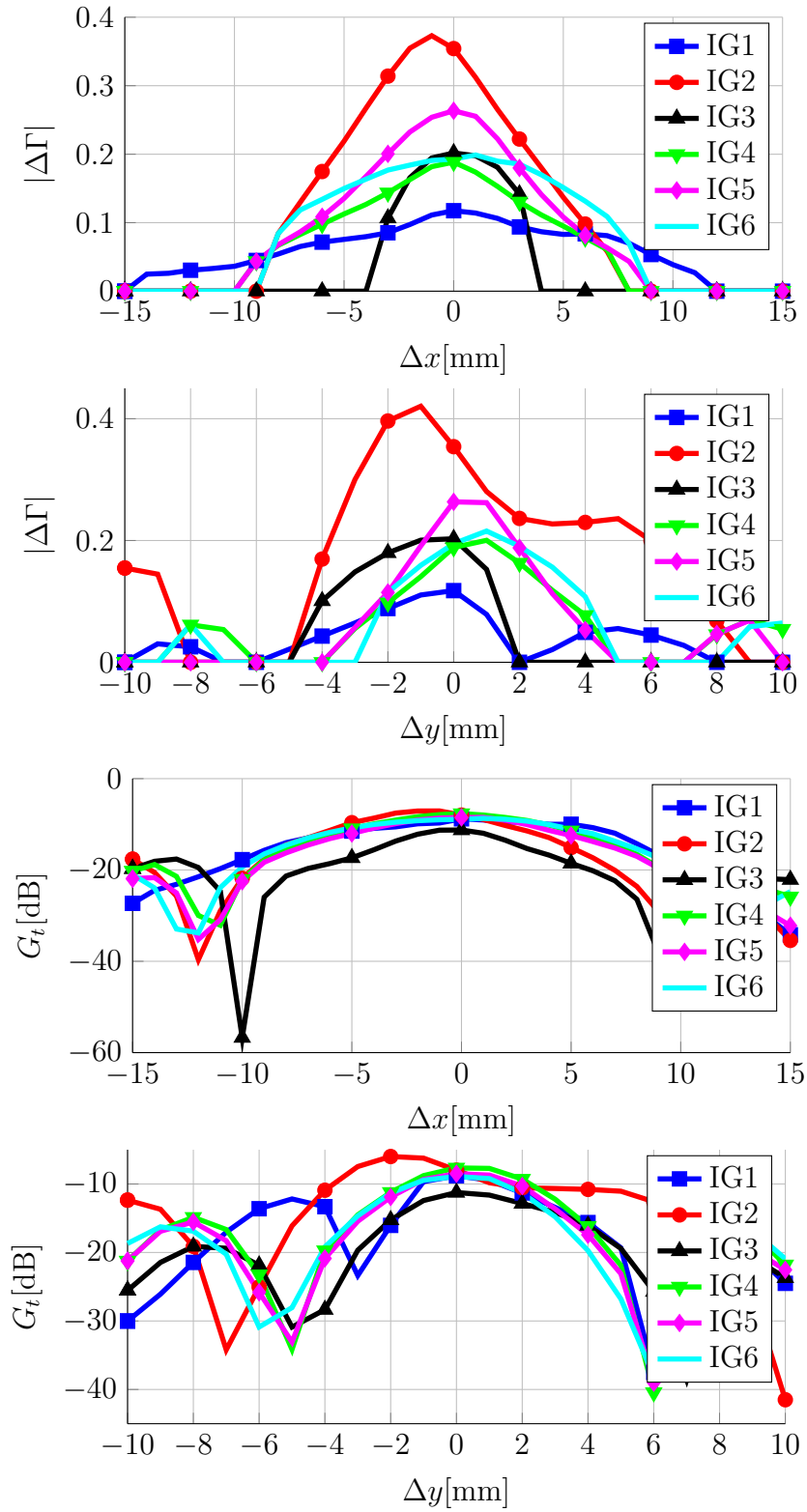
Another observation is the simultaneous coupling from a relatively long coupler loop to the inductive loop and radiator of the inlay in the CG3/IG3 and CG4/IG3 cases (Fig. 6.2 and 6.4). The high threshold power levels indicate destructive interference. The conclusion is that the size of the DTLL has importance.

In Figure 6.8 motion swept measured $|\Delta\Gamma|$ at 0 dBm input power is compared with simulated coupling (G_t), for CG1. The motion sequence is illustrated in the right of Figure 6.6. The relative zero positions are given by the crosses in Figure 6.2 and 6.4. These are also the positions of highest simulated power gain for the CG1 geometry.

The results in Fig. 6.8 show that the measured focal points in $|\Delta\Gamma|$ agree well with linear simulations of coupling, and provide some spatial margin in the xy -plane.

The spatial directivity is an important parameter. The DTLL is regarded as an element suitable for array configurations, being part of future work. The optimization of the DTLL itself will also be part of future work, but already the initial study with the results presented in Paper D suggests the DTLL as being a promising candidate for efficient coupling elements. In an array configuration one or several elements may be used as active groups for coupling were the spatial margin of one element is still satisfactory, as to enable a homogeneous magnetic field for coupling. This concept is also not limited to a one dimensional solution, but selectivity may also be achieved in two dimensions, where the phase compensation theory developed in C may be used. This however is not independent of the bandwidth of the DTLL itself, a component optimization problem.

As compared with the results in Paper C a better control of spatial selection can be achieved, by splitting up the problem in efficient coupling elements instead. TRL based solutions have high absorbing power terminations of the feeding current, with lower efficiency in coupling. Hence, internal losses are higher than for a DTLL. This is despite the fact that TRL based solutions have better return loss performance over a broader range of frequencies. From the discussion in Section 4.3, the $|\Delta\Gamma|$ -value is a good indicator of high efficiency, when RFID transponders are considered. The shunt connected resistance of $500\ \Omega$ ($R_{i,min}$) used in Paper D leads to a significantly lower internal power consumption in the DTLL than a terminating resistor in a TRL coupler.

Figure 6.8: Motion swept $|\Delta\Gamma|$ and transducer gain for CG1.

Chapter 7

Conclusions and future work

A big part of this thesis is the development of FOM theory for RFID transponder chips. The purpose was to find a rigid characterization method and performance measure on transponders, out of the black box perspective. Focus is put on common behaviour among the entire family of transponders. The reason is that in the long term completion of this project robust coupler solutions are targeted, which perform independent of the transponder types, as long as it is an RFID transponder. The combination of mismatch behaviour and $|\Delta\Gamma|$ -value swept over delivered power and considered as function averages, to take into account an arbitrary source impedance proves to give interesting results. RFID-profiling behavior found in printer tests is mainly explained and deviations between different chip types are seen.

The research project develops to consider efficient coupling structures, where phase compensation as part of the more general concept of phase manipulation, is touched, by considering the segmented transmission line. Phase manipulation will be future work in array configurations of coupling elements. The theory is independent of what type of coupling element is considered.

The differential transmission loop (DTLL) as candidate for efficient reactive near field (RNF) coupling towards RFID inlays is explored and a proof of concept is established. The DTLL has promising performance in RNF programming of RFID inlays, shown in the measurement of the $|\Delta\Gamma|$ -value and the results agree with FEM simulations.

Future work will be concerned with the optimization of the DTLL itself and the array configuration of the DTLL. The work will be divided into three parts. The first part deals with the field theoretic problem of optimizing the loop geometry to be compatible with a larger family of inlays. In the second part, the differential feeding of the DTLL will be investigated more in depth to see what the compromise between bandwidth and spatial resolution (size/number of elements) will be. This is basically a component optimization problem. The third part will be the array implementation of the DTLL with adaptation, to achieve the final solution of adaptive RFID programming. Regulatory circuit concepts and fabrication are also included in this part.

Appendix A

A short review of the RFID protocol

The measurement of transponder impedance within a pulse relies on the triggering of a wake-up signal with certain timing properties, which are specified in the GS1 Class-1 Generation-2 RFID protocol specification, shortly named Gen2 [2]. The wake up signal is implemented in the measurement system as a pulse profile. In this appendix a short review of critical parameters is made for the reader to get more familiar with what is implemented in the measurement system. The theory described in this section along with terms and their numeric values are extracted from Gen2. The electrical requirements on the RF envelope transient conditions, such as rise time, settling time, overshoot, undershoot etc. are not covered. These are parameters not being critical since data is always captured within a pulse, i.e., no transient conditions are present. For further details the reader is referred to the Gen2 specification.

A.1 Baseband

The basic reference for timing is the type A reference interval, T_{ari} , which is the $Data_0$ length. This means that all other timing parameters have the T_{ari} value as basic building block along with tolerances. Since timing parameters are not fixed but rather reside within intervals information initially needs to be transferred to the transponder. This would be equivalent with the situation where a passive inlay in a non-energized state enters an RF energizing field. This is done by the Query command which initiates an inventory round. The Query command is pre-pended with a preamble, which contains the timing information. Values of the timing parameters are summarized in Table A.1.

The envelope of the Preamble is shown in Fig. A.1. Also shown in Fig. A.1 are the $Data_0$ and $Data_1$ symbols.

High levels represent carrier wave (CW) on and low levels CW off. The difference is essentially the duration of CW on. The pulse width (PW) is the duration of CW

Table A.1: Baseband timing parameters.

Parameter	Min	Max	Unit
$Tari$	6.25	25	μs
$Data_1$	1.5	2	$Tari$
Del (Delimiter)	11.875	13.125	μs
$RTCAL$	2.5	3	$Tari$
$TRCAL$	1.1	3	$RTCAL$

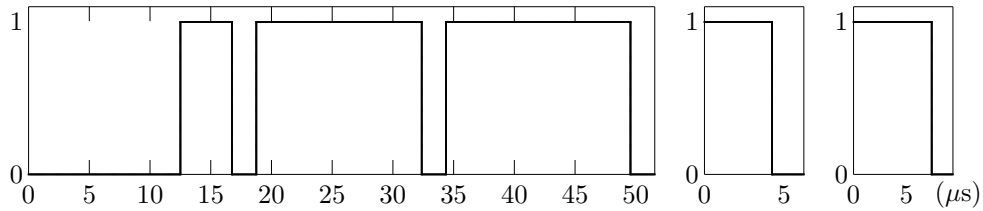


Figure A.1: Base band symbols. Left: Preamble. Right: Data0 and data1 symbols.

off after the transition from high to low. It is required to reside within the interval

$$PW \in [\max(0.265Tari, 2), 0.525Tari]. \quad (A.1)$$

Note that the $RTCAL$ length is always the sum of $Data_0$ ($= 1 Tari$) and $Data_1$ lengths. The Preamble consists of the Del , $Data_0$, $RTCAL$ and $TRCAL$ in sequence. The transponder measures the length of $RTCAL$ and divides it by two. This pivot is then used as decision criteria for subsequent symbols being $Data_0$:s or $Data_1$:s.

A.2 Wake-up signal

Gen2 specifies the command structure for reading and writing operations to the transponder chip. These sub commands are the building blocks of all higher level commands implemented in any interrogator conforming to the specification. Since Paper B focuses on the measurement of low and high level impedance states in the transponder, only the least necessary sub commands are implemented in order to trigger the transponder. The command which will be used is the Query command:

$$\underbrace{1000}_1 | \underbrace{0}_2 | \underbrace{00}_3 | \underbrace{0}_4 | \underbrace{0}_5 | \underbrace{00}_6 | \underbrace{0}_7 | \underbrace{0000}_8 | \underbrace{10111}_9. \quad (A.2)$$

The different groups are explained in Table A.2.

The initial signaling from interrogator to transponder consists of the Query command pre-pended by the preamble explained in Section A.1. In this command sequence all the data needed for the transponder to set up the backscatter signal is contained. The transponder will always give a reply, provided the transponder is

Table A.2: The Query command.

Group	Value (binary)	Meaning
1	1000	command name
2	0	$DR = \frac{64}{3}$ (divide ratio)
3	00	$M = 1$ (FM0)
4	0	no pilot tone
5	0	sel:all
6	0	session: S0
7	0	target: A
8	0	$Q = 0$
9	10111	CRC-5

allowed to respond. In a multi transponder environment, an anti collision algorithm is implemented determining in what order each transponder, one at a time, will respond. Only one at a time can respond or a fault occurs. The Q -value is used for the anti collision algorithm. Basically a high value corresponds to a big population of inlays. In the measurements of Paper B, only one transponder is located in the energizing field, which will imply an immediate response. Therefore $Q = 0$ always.

The divide ratio (DR) is used for the transponder to calculate the back scatter link frequency as $f_{BLF} = DR/TRcal$. The maximum value is chosen. A subcarrier is used for spectrum enhancements in dense interrogator environments. Specifically, in an RFID printer environment with a single interrogator this is not applicable so $M = 1$ always.

A.3 Estimation of maximum required recording time

In Paper B the complete period of events that is considered occur as half duplex communication. This means that the measurement system issues a command sequence, realized as a pulse train. After some time the transponder will reply back by modulating the reflection of the carrier, shifting between two distinct impedance states. The exact time until transponder reply is not known. However, the measurement system used in Paper B has a recording time which can be considered as long. The whole period of events may be repeated under different electrical conditions, such as RF power and carrier frequency. As an estimate for the maximum pulse generation period all parameters described previously are maximized according to Gen2. The period or link timing can be expressed as

$$T = t_{pr} + t_{QUERY} + t_{CW,1} + t_{reply} + t_{CW,2} \quad (\text{A.3})$$

where

$$\begin{aligned}
 t_{pr} &= Del + Tari + RTcal + TRcal \\
 t_{QUERY} &= 15Tari + 6Data_1 \\
 t_{CW,1} &\in \max \left(RTcal, 10 \frac{TRcal}{DR} \right) [0.85, 1.15] \\
 &\quad + [-2, +2] \mu s \\
 t_{reply} &= 23 \frac{TRcal}{DR}, \quad t_{CW,2} \in [3, 20] \frac{TRcal}{DR}.
 \end{aligned} \tag{A.4}$$

t_{QUERY} is based on the number of symbols in (A.2). t_{reply} is based on the six symbol FM0-preamble, 16 symbol RN16 and *dummy1* symbol according to Gen2. Maximizing (A.4) according to Table A.1 yields a maximum pulse generation period of roughly $T_{max} = 1.6$ ms.

In the measurement system of Paper B the described link timing defines a single sweep in the vector network analyzer. The RN16 is a random based sequence, issued by the transponder. It would then be impossible to measure the impedance within a pulse for these symbols. However, the FM0-preamble is fixed, although the timing resides within intervals specified by the protocol. Yet still, the pulse time is long enough as to capture stable values of complex impedance over sweeps. Hence, the FM0-preamble serves as impedance data set. An averaging over sweeps is done in a post analysis process.

A.4 Minimum required system bandwidth

The reference for calculation of the required bandwidth is the timing of the transponder reply. From Gen2 the FM0 baseband signal has a minimum duty cycle of 45%. The shortest pulse width in the transponder reply, is obtained from the maximum backscatter link frequency by choosing the minimum value of $TRcal$ in Table A.1, given as $2.75 Tari_{min} = 17.2 \mu s$. By taking into account the duty cycle and $DR = 64/3$, the minimum pulse length to be resolved is $0.36 \mu s$ which roughly corresponds to a required system bandwidth of 2.8 MHz.

Appendix B

Circle theory

Circle theory for bilinear mappings in the complex plane is a well developed subject and used frequently in this thesis [25, 37]. Properties of passive loads and mismatch are of interest here. Initially a short review of the general theory is given.

A circle of radius r and with center located at a point C in the complex plane can in compact and expanded form, respectively, be described as

$$|z - C| = r \quad |z|^2 - zC^* - z^*C = r^2 - |C|^2. \quad (\text{B.1})$$

A bilinear mapping from the z -plane to the w -plane is of the form

$$w = \frac{az + b}{cz + d} \quad (ad - bc \neq 0). \quad (\text{B.2})$$

Again expanding (B.2) with the restriction $|w| = \alpha$, a constant, will lead to the same form as (B.1), in this case with radius and center, respectively given as

$$C = \frac{\alpha^2 c^* d - a^* b}{|a|^2 - \alpha^2 |c|^2} \quad r = \frac{\alpha |ad - bc|}{\left| |a|^2 - \alpha^2 |c|^2 \right|}. \quad (\text{B.3})$$

This derivation was for the circle in the w -plane having its center at the origin. In the case when the center is located at a point w_0 the small ruse is used according to

$$w - w_0 = \frac{az + b}{cz + d} \iff w = \frac{(a - cw_0)z + b - dw_0}{cz + d} \quad (\text{B.4})$$

where in this case the old a and b are replaced by $a - cw_0$ and $b - dw_0$, respectively upon which (B.3) may be used. It is concluded that the final recipe for the mapping of one circle, $\{C_a, r_a\}$, into another, $\{C_b, r_b\}$, by means of the bilinear mapping (B.2) will be

$$C_b = \frac{r_a^2 c^* d - (a - cC_b)^* (b - dC_a)}{|a - cC_a|^2 - r_a^2 |c|^2} \quad r_b = \frac{r_a |ad - bc|}{\left| |a - cC_a|^2 - r_a^2 |c|^2 \right|} \quad (\text{B.5})$$

Appendix C

Graphical user interfaces

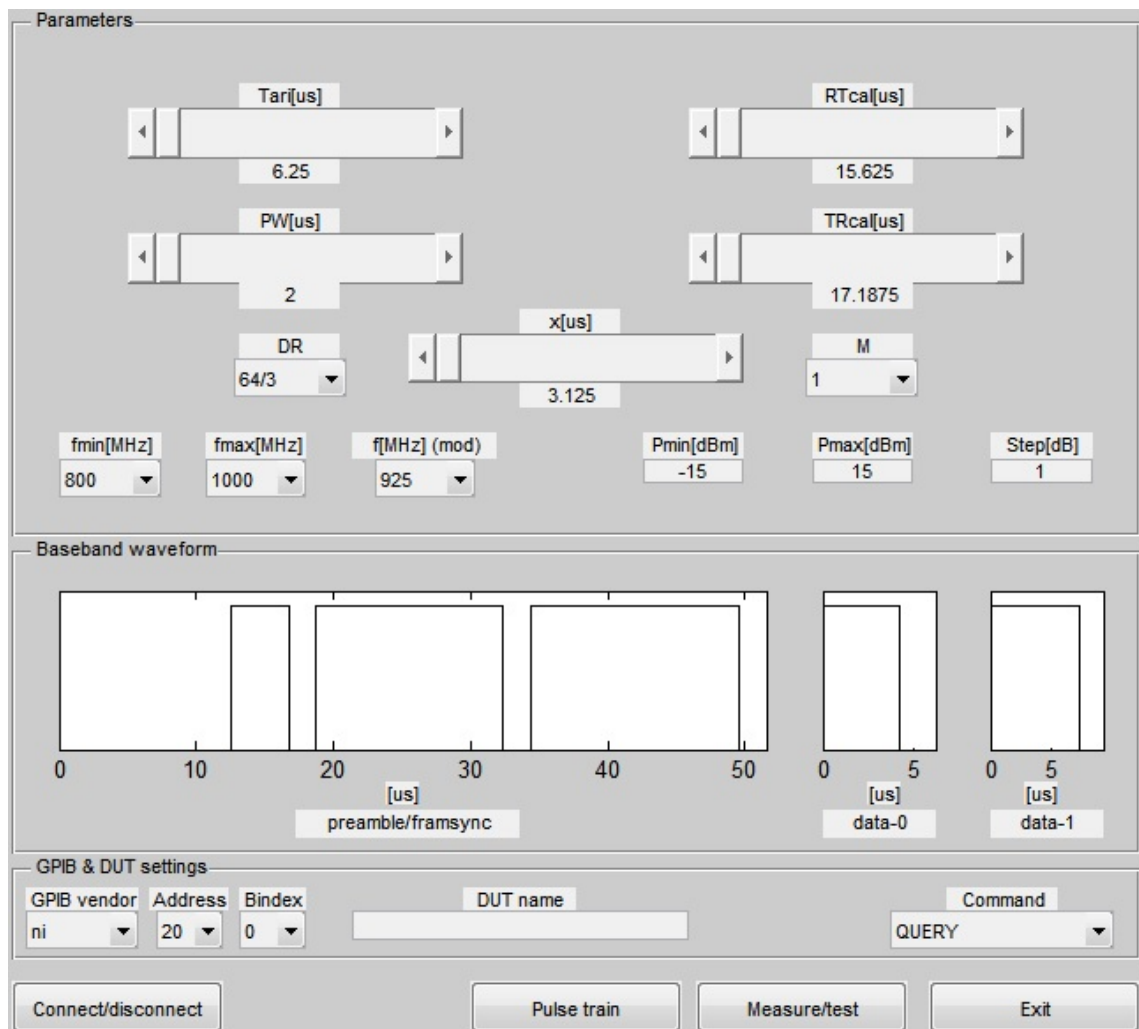


Figure C.1: RFID application GUI.

In Paper B transponder chips from several vendors with several individuals of each are measured. Many repetitive moments are required. MATLAB offers a

vast functionality for the design of graphical user interfaces (GUI), with an easy to implement control of R&S instrumentation. This is utilized to program an application/measurement GUI, shown in Figure C.1

The major functionality that is provided consists of the baseband signal design, initialization of the GPIB connection, and start of measurement sweeps using SCPI commands. The baseband signal may be arbitrarily designed, where the timing parameters are constrained to intervals specified by Gen2 [2]. Except calibration of the ZVA/ZVAX, which is a manual step, the instruments are run remotely during the entire measurement.

After a measurement sweep has been completed, using any of the combinations listed in Section 3.6.1, data is stored on the host PC. Since data is not averaged in the VNA, a partially manual post analysis procedure is needed before the final quantities can be calculated. The reason for the external post analysis is the removal of dead sweeps. Otherwise the average would be erroneously calculated. A MATLAB GUI was also programmed for post analysis, shown in Figure C.2.

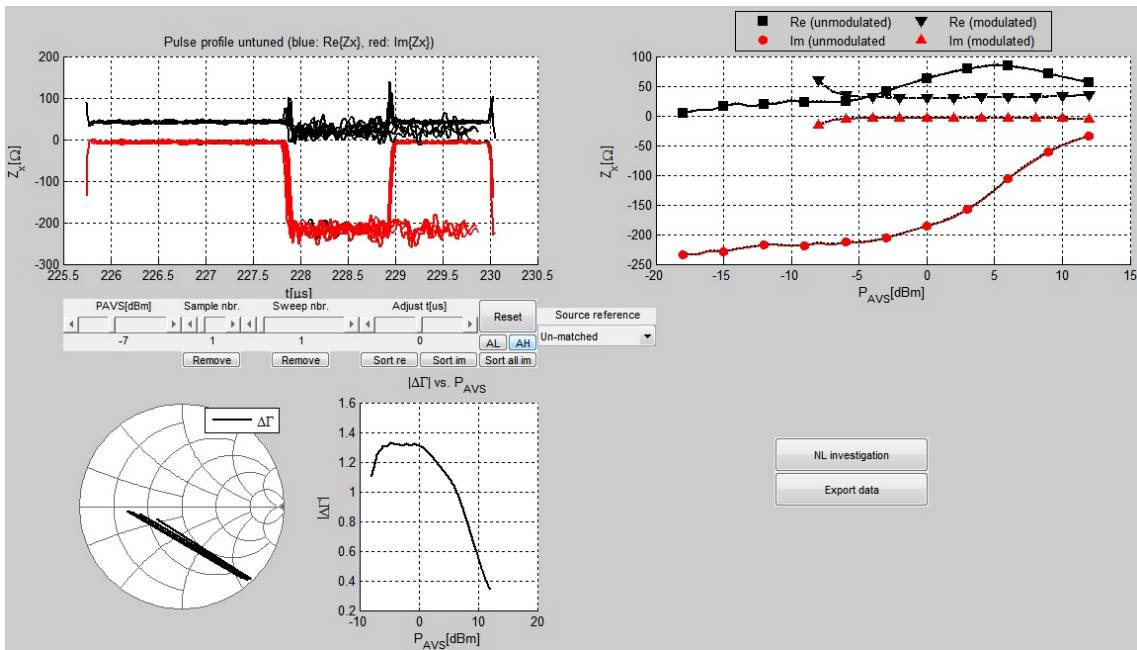


Figure C.2: GUI for the post analysis.

One of the important features in the post analysis GUI is the sorting of pulse profile samples. An algorithm for adding time offsets has been implemented. The sorting is done separately for real and imaginary data, using the identical algorithm. Hence, it suffices to only take the imaginary part as example. In practice it is observed that the biggest change in impedance for the transfer from low to high pulse state occurs for the imaginary part, making the imaginary part algorithm the most used. The algorithm is implemented as follows. The pulsed reactance data is stored in an $M \times N$ matrix $X = (x_{kl})$, where M is the number of sweep points in time and N is the number of sweep samples. Let $X_{min} = \min(X)$ and $X_{max} = \max(X)$

be the minimum and maximum value of reactance in X , respectively. The pivot $\bar{X} = (X_{min} + X_{max}) / 2$, is then used as threshold value for the assignment of ones or zeros, according to

$$x_{norm,kl} = \begin{cases} 0, & x_{kl} \leq \bar{X} \\ 1, & x_{kl} > \bar{X} \end{cases}, \quad k, l \in [M \times N]. \quad (C.1)$$

The result is a an $M \times N$ matrix $X_{norm} = (x_{norm,kl})$ with only zeros and ones, serving as indicators for low and high impedance state, respectively. The first column of X_{norm} , $X_{norm,1}$ is now used as reference, where the flipped versions of the remaining columns, $X_{norm,k}$, $k = 2, 3, \dots, N$, are being convolved with the reference

$$C_k = \left(x_{norm,Mk}, x_{norm,(M-1)k}, \dots, x_{norm,2k}, x_{norm,1k} \right)^t * X_{norm,1}, \quad k = 2, 2, \dots, N. \quad (C.2)$$

C_k is an $2M - 1$ vector, which will have a maximum value at indices $i_{k,max,l}$, $l = 1, 2, \dots, L$. Note that usually the maximum value is not unique. Further, $i_{k,max,l} > M$ is possible. The chosen value $i_{k,max}$ is taken as

$$i_{k,max} = \begin{cases} i_{k,max,l}, & \max_l (i_{k,max,l}) > M \\ i_{k,max,1}, & \text{else.} \end{cases} \quad (C.3)$$

If the minimum time step in the sweep is δt , the time offset for each sample is finally calculated as $\Delta t_k = i_{k,max} \delta t$.

Bibliography

- [1] K. Finkenzeller, *RFID Handbook: Fundamentals and Applications in Contactless Smart Cards, Radio Frequency Identification and Near-Field Communication*. Hoboken, NJ, USA: Wiley, 2010.
- [2] GS1 EPCGlobal Inc., “EPC™ Radio-Frequency Identity Protocols Class-1 Generation-2 UHF RFID,” April 2015.
- [3] B. Y. Tsirlin, “UHF RFID Antennas for Printer-Encoders Part 1,” *High Frequency Electronics*, vol. 6, no. 9, pp. 28–39, September 2007.
- [4] B. Y. Tsirlin, “UHF RFID Antennas for Printer-Encoders Part 2,” *High Frequency Electronics*, vol. 6, no. 10, pp. 36–45, October 2007.
- [5] B. Y. Tsirlin, “UHF RFID Antennas for Printer-Encoders Part 3,” *High Frequency Electronics*, vol. 6, no. 11, pp. 18–25, November 2007.
- [6] M. Frank, “Magnetic RFID Coupler With Balanced Signal Configuration,” US Patent 8,022,815, 2011.
- [7] L. M. Chiu, “Capacitively-Coupled RFID Encoder,” US Patent 7,348,885, 2008.
- [8] B. Y. Tsirlin, M. Tian, and K. Torchalski, “Near Field Coupling Devices and Associated Systems and Methods,” US Patent 8,791,874, 2014.
- [9] GGB Industries, inc., Naples, FL 34101, USA, <http://www.ggb.com>, February 2016.
- [10] R. F. Bauer and P. Penfield, “De-embedding and Unterminating,” *IEEE Transactions on Microwave Theory and Techniques*, vol. MTT-22, no. 3, pp. 282–288, March 1974.
- [11] L. W. Mayer and A. L. Scholtz, “Sensitivity and Impedance Measurements on UHF RFID Transponder Chips,” in *The Second International EURASIP Workshop on RFID Technology*, 2008, pp. 1–10.
- [12] C. A. Balanis, *Antenna Theory: Analysis and Design*, 3rd ed. Wiley, May 2005.
- [13] P. V. Nikitin, K. V. S. Rao, and S. Lazar, “An Overview of Near Field UHF RFID,” in *2007 IEEE International Conference on RFID*, 2007, pp. 167–174.

-
- [14] J. P. Curty, N. Joehl, C. Dehollain, and M. J. Declercq, "Remotely Powered Addressable UHF RFID Integrated System," *IEEE Journal of Solid-State Circuits*, vol. 40, no. 11, pp. 2193–2202, November 2005.
- [15] A. Facen and A. Boni, "A CMOS Analog Frontend for a Passive UHF RFID Tag," in *Proceedings of the 2006 International Symposium on Low Power Electronics and Design*, 2006, pp. 280–285.
- [16] J. Essel, D. Brenk, J. Heidrich, and R. Weigel, "A Highly Efficient UHF RFID Frontend Approach," in *IEEE MTT-S International Microwave Workshop on Wireless Sensing, Lokal Positioning and RFID (IMWS 2009 - Croatia)*, 2009, pp. 1–4.
- [17] C.-H. Loo *et al.*, "Chip Impedance Matching for UHF RFID Tag Antenna Design," in *Progress In Electromagnetics Research*, vol. 81, 2008, pp. 359–370.
- [18] P. V. Nikitin, K. V. S. Rao, R. Martinez, and S. F. Lam, "Sensitivity and Impedance Measurements of UHF RFID Chips," *IEEE Transactions on Microwave Theory and Techniques*, vol. 57, no. 5, pp. 1297–1302, May 2009.
- [19] A. Ghiotto, T. P. Vuong, and K. Wu, "Chip and antenna impedance measurement for the design of passive UHF RFID tag," in *2010 European Microwave Conference (EuMC)*, 2010, pp. 1086–1089.
- [20] H. Yojima, Y. Tanaka, Y. Umeda, O. Takyu, M. Nakayama, and K. Kodama, "Dynamic Impedance Measurement of UHF Passive RFID Tags for Sensitivity Estimation," in *2010 International Symposium on Communications and Information Technologies (ISCIT)*, 2010, pp. 344–349.
- [21] G. A. Vera, Y. Duroc, and S. Tedjini, "RFID Test Platform: Nonlinear Characterization," *IEEE Transactions on Instrumentation and Measurement*, vol. PP, no. 99, 2014.
- [22] J. Essel, D. Brenk, J. Heidrich, R. Weigel, and D. Kissinger, "Large-Signal Measurements and Nonlinear Characterization of an Analog Frontend for Passive UHF CMOS RFID Transponders," *IEEE Transactions on Microwave Theory and Techniques*, vol. 61, no. 2, pp. 948–959, February 2013.
- [23] E. V. Damme, J. Verspecht, F. Verbeyst, and M. V. Bossche, "Large-Signal Network Analysis - A Measurement Concept to Characterize Nonlinear Devices and Systems," Agilent Technologies, Tech. Rep., 2002.
- [24] D. G. Kuester, D. R. Novotny, J. R. Guerrieri, and Z. Popović, "Simple Test and Modeling of RFID Tag Backscatter," *IEEE Transactions on Microwave Theory and Techniques*, vol. 60, no. 7, pp. 2248–2258, July 2012.
- [25] G. Gonzalez, *Microwave Transistor Amplifiers*. Prentice Hall, 1997.
- [26] S. C. Cripps, *RF Power Amplifiers for Wireless Communications*. Artech House, 1999.

-
- [27] G. De Vita and I. G., "Design Criteria for the RF Section of UHF and Microwave Passive RFID Transponders," *IEEE Journal of Solid-State Circuits*, vol. 38, no. 10, pp. 1602–1608, October 2005.
- [28] U. Karthaus and F. M., "Fully Integrated Passive UHF RFID Transponder IC With 16.7- μ W Minimum RF Input Power," *IEEE Journal of Solid-State Circuits*, vol. 38, no. 10, pp. 1602–1608, October 2003.
- [29] S. A. Maas, *Nonlinear Microwave and RF Circuits*. Artech House, 2003.
- [30] M. Abramowitz and I. A. Stegun, *Handbook of Mathematical Functions*. New York: Dover, 1970.
- [31] L. Råde and B. Westergren, *Mathematics Handbook for Science and Engineering BETA*. Studentlitteratur, 1995, vol. 3.
- [32] K. Kurokawa, "Power Waves and the Scattering Matrix," *IEEE Transactions on Microwave Theory and Techniques*, vol. 13, no. 2, pp. 194–202, September 1965.
- [33] Rohde & Schwarz, <http://rohde-schwarz.com>, April 2015.
- [34] IEEE, "IEEE standard for higher performance protocol for the standard digital interface for programmable instrumentation," *IEEE Std 488.1-2003 (Revision of IEEE Std 488.1-1987)*, pp. 1–140, Dec 2003.
- [35] Maury Microwave, <https://www.maurymw.com>, April 2015.
- [36] C. Caloz and T. Itoh, "Application of the transmission line theory of left-Handed (LH) materials to the realization of a microstrip "LH line"," in *Antennas and Propagation Society International Symposium, 2002. IEEE*, vol. 2, 2002, pp. 412–415.
- [37] R. E. Collin, *Foundations for Microwave Engineering*. McGraw-Hill, 1992.
- [38] D. Kuylenstierna and P. Linnér, "Design of Broad-Band Lumped-Element Baluns With Inherent Impedance Transformation," *IEEE Transactions on Microwave Theory and Techniques*, vol. 52, no. 12, pp. 2739–2745, December 2004.